INL/-EXT-19-55851
Revision 3

Engineering & Microstructure Scale PIE Report on EBR-II X441A Metallic Fuel Pins for the MORPH Experiment

July 2022

Nuclear Science User Facilities

Luca Capriotti, Karen Wright, Fidelma Di Lemma, Tammy Trowbridge,
Idaho National Laboratory

Assel Aitkaliyeva, Thaddeus T. Rahn,
University of Florida

Idaho National Laboratory

INL is a U.S. Department of Energy National Laboratory
operated by Battelle Energy Alliance, LLC

INL/-EXT-19-55851
Revision 3

Engineering & Microstructure Scale PIE Report on EBR-II X441A Metallic Fuel Pins for the MORPH Experiment

Nuclear Science User Facilities

Luca Capriotti, Karen Wright, Fidelma Di Lemma, Tammy Trowbridge,
Idaho National Laboratory
Assel Aitkaliyeva, Thaddeus T. Rahn,
University of Florida

July 2022

Idaho National Laboratory
Idaho Falls, Idaho 83415

http://www.inl.gov

Prepared for the
U.S. Department of Energy
Office of Nuclear Energy
Under DOE Idaho Operations Office
Contract DE-AC07-05ID14517

Page intentionally left blank

CONTENTS

FIGURES

TABLES

Page intentionally left blank

Engineering & Microstructure Scale PIE Report on EBR-II X441A Metallic Fuel Pins for the MORPH Experiment

1. INTRODUCTION

The objectives of this project are to increase fundamental understanding of irradiation-induced metallic U-Pu-Zr fuel behavior and to obtain data needed for the development of irradiation models for metallic fuels in MARMOT.

The requested metallic fuel pins are from the X441A experiment irradiated in Experimental Breeder Reactor (EBR)-II and will be provided by the PIs for the duration of the experiment. The purpose of the pins irradiated in the X441A assembly was to vary Zr composition and fuel slug diameter in order to provide data for the metallic fuel performance code "LIFEMETAL" [ANL-IFR-125]. The fuels of interest to this project are metallic fuels with several Zr compositions (in wt.%): U-19Pu-6Zr, U-19Pu-10Zr, and U-19Pu-14Zr, which were irradiated to a peak burnup of approximately 11 at.%. The cladding was the same for all three fuel pins (austenitic stainless steel D9), which allows investigation of fuel-cladding interaction (FCI) phenomena. Varying Zr content in fuel pins enables investigation of the effect of Zr on fuel restructuring and fuel-cladding compatibility. Engineering and microstructure scale PIE activities will be focused on investigation of fundamental aspect of fuel performance such as species diffusion and migration, fission product behavior, and constituent redistribution. Obtained microstructural information will be used as the basis for the development of MARMOT models of U-Pu-Zr fuel performance at the mesoscale.

Experimental data obtained through this proposal will be used to provide this fundamental understanding which will serve as the foundation of the development of radiation models for U-Pu-Zr in MARMOT. It will also provide a starting point for the design of new experiments to provide data for the validation of these MARMOT models.

2. IRRADIATION HISTORY AND EXPERIMENT CHARACTERISTICS

The fuel pins of interest were fabricated by injection casting, and they were irradiated in EBR-II as part of DP-1 test, which was a 61-pin bundle steady-state irradiation experiment designed to determine the effects of fuel-element design parameters on fuel behavior. Peak fuel pin conditions for the test pins at beginning of irradiation (BOI) (calculated) were 53 kW/m and 595°C cladding temperature. End of irradiation EOI conditions were 47 kW/m and 560°C cladding temperature [1]. Three pins were irradiated at average (calculated) burnups of 9, 10.3, 11.5 at%, respectively. The fuel design parameters included varying Zr content, plenum/fuel volume ratio, fuel smear density, and cladding thickness. The objectives of the DP-1 test were to: 1) determine the design envelope of integral fast reactor (IFR) fuel elements for satisfactory performance, 2) provide input for optimization of IFR fuel designs, and 3) generate data for validating fuel pin performance codes. The primary cladding was HT-9, with a small number of D9-clad pins. The austenitic D9 was a backup cladding material in the IFR design concept, and the goal was to compare fuel-cladding compatibility with similarly designed HT-9 fuel pins. For the objectives of this project, 3 fuel pins (A797, A812, A814) have been selected that are D9 cladding and with 3 different alloys varying Zr.

Table 1 reports the description of the fuel pins [2].

Table 1. X441A experiment pins description [2].

X441A	A797/A812/A814
Composition	U-19Pu-6/10/14Zr
Pin diameter	0.23 in
Fuel diameter*	0.173 in
Fuel column height*	13.5 in
Plenum gas	75% He + 25% Ar
Tag gas	Xe
Smear density	75%
Cladding	D9
Cladding thickness	0.015 in
Av burnup reached	9/10.3/11.5
*Nominal dimensions are considered in this table. The as-cast dimensions have some variability within the casting specification.	

Post irradiation characterization of these specific fuel pins has been conducted in the past (in the extend of neutron radiography and profilometry), and other sibling metallic fuel pins from the DP-1 experiment subassembly have been examined. This report summarizes the new data acquired as part of the NSUF MORPH project, which is compared to old data collected on the 3 pins and other older data from the DP-1 experiment.

3. NON-DESTRUCTIVE EXAMINATIONS

A series of non-destructive examinations were performed on the selected fuel pins. These exams included visual examination, neutron radiography, gamma spectrometry scans, and inspection for changes in dimension. These exams are designed to generally evaluate fuel performance and highlight areas of the fuel that need to be examined in further detail.

3.1 Visual Exams

Visual examinations were performed through the hot-cell windows. Observations by the hot-cell staff were used to positively identify the pins after retrieval by the identification numbers located on the end caps. Nothing unusual was observed on the pins during visual examination. End fittings were placed on the pins to facilitate handling in the hot-cell and increase their compatibility with different hot-cell equipment. The as-retrieved state was recorded utilizing through-window digital photography. An example of image is shown in Figure 1 while the pins have been placed in the holder for neutron radiography imaging. There are no obvious visual defects apparent in the pins. It is possible to see the wire wrap used in EBR-II fuel pins present on the first two from the left-hand side, and there is no wire wrap on the pin on far right (A814). It was removed prior to this PIE campaign.

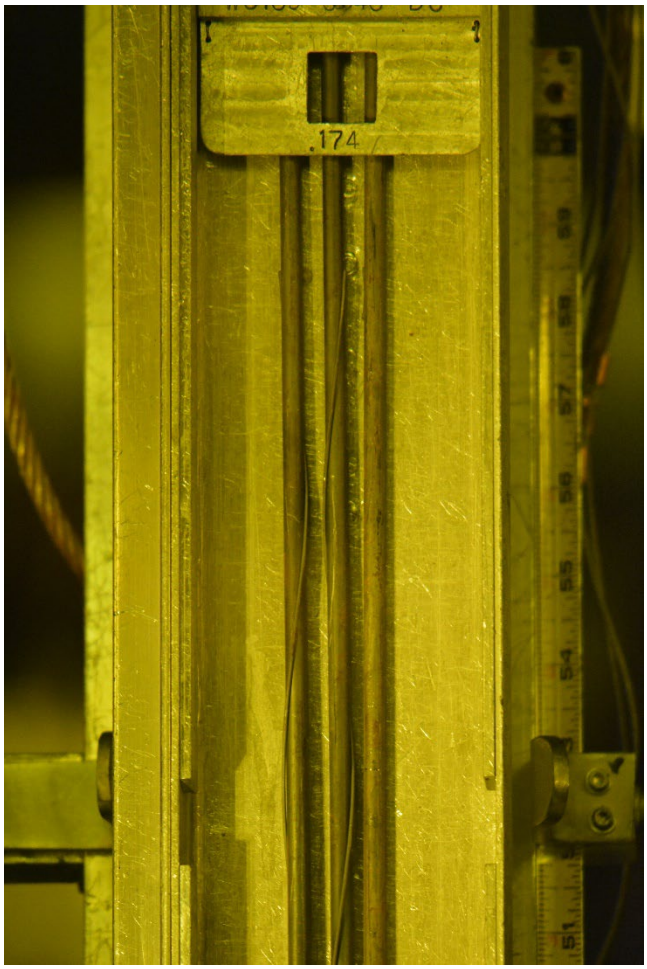

Figure 1. Example of visual exam on the X441A fuel pins. From left to right: A797, A812, A814.

3.2 Neutron Radiography

Neutron radiography was performed using the Neutron Radiography Reactor (NRAD) located in the basement of hot fuel examination facility (HFEF). The NRAD reactor is a 250kW TRIGA reactor with two beam lines. The east beam line services a position below the main floor of the hot cell and is used for irradiated fuel. Neutrons pass through the fuel specimen and expose different activation foils.

Neutron radiography images were taken of the 3 pins at several angles with both a dysprosium (Dy) foil for thermal neutron radiography and a Cd-covered indium (In) foil for epithermal neutron radiography.

In the thermal neutron radiography (Figure 2) a small amount of material dissolved in the bond sodium above the fuel column is visible for all the three pins (usually called “sodium plug”) and some sodium-fuel interaction might have taken place and/or a “foam” structure exist. Epithermal image in Figure 3 revealed that the fuel does not appear to have begun to creep down into the void space associated with the bottom end plug, but there is some evidence of lift-off on A797. Furthermore, there is a drop-in neutron attenuation all along the center of the three fuel columns except at the top of the fuel pin where sodium – fuel interaction might take place. This is an indication of density change and/or constituent redistribution due to a depletion of neutron resonance capture isotopes (likely actinides) in the center of the fuel.

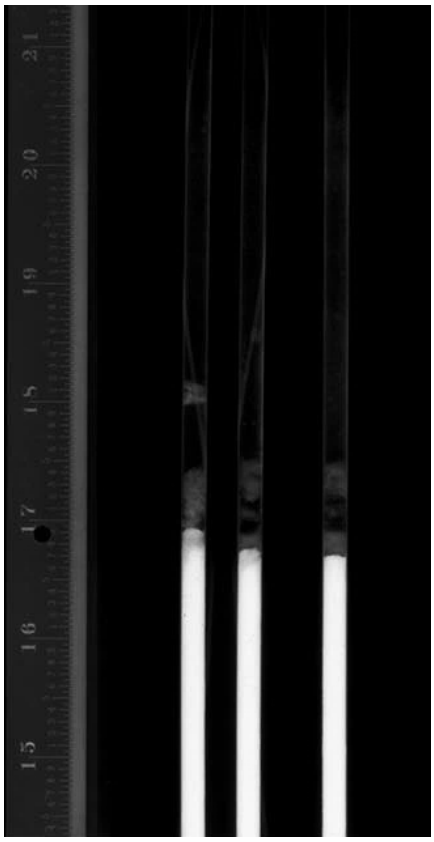

Figure 2. Thermal neutron radiography of the top of the fuel pins where the “sodium plugs” are visible.

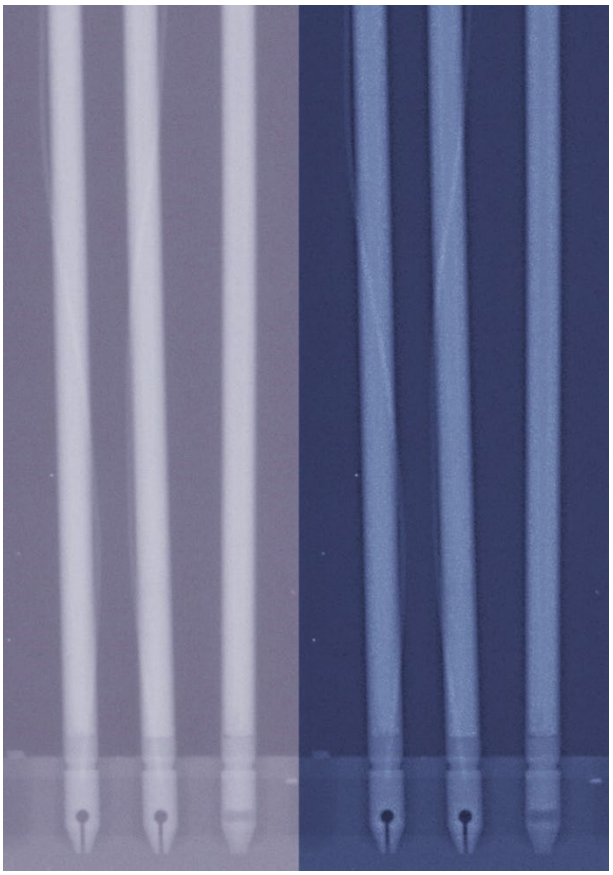

Figure 3. Epithermal neutron radiography (right) and enhanced contrast and color image (left) from the bottom of the fuel pins. On the pin on far right-hand side (pin A814) a small lift off is presence and in all three a drop-in neutron attenuation in the center of the fuel columns is also visible.

The quantitative measurement generally obtained from neutron radiography of irradiated fuels is axial growth of the fuel column. These results are reported in Table 2 along with the old data collected.

The results would suggest an increase of axial growth in direct correlation with the decrease of Zr content, in contrast with the old data in which the axial growth is basically the same for the three different alloys. The majority of the axial growth in a metallic fuel system happens in the unrestrained condition until contact with the cladding is made (around 2 at% burnup) [3–5]. The relationship between elements' redistribution-fission gas release-swelling-restructuring is not trivial, and change in the Zr content may affect this system.

Furthermore, there is a lack of consensus among experts concerning how to understand the phenomenon of axial growth in metallic fuels. There is some evidence that suggests axial growth in metallic fuel may be, in part, an end effect that happens near the unconstrained, free fuel surface at the top of the fuel column. For example, measured axial growths in fast flux test facility (FFTF) irradiations of metallic fuel have been noted to be less than those for identical compositions in EBR-II [6]. Compared to the literature for U-(0 to 26)Pu-10Zr [4], the values reported here are still in agreement. More study is needed for a more comprehensive understanding of this phenomena.

Table 2. Axial growth of the three fuel pins X441A measured in this work and comparison with historical data (listed as sibling pins).

X441A fuel pin	Composition	Axial growth	Axial growth (Sibling Pins)
A797	U-19Pu-6Zr	3%	1.88%
A812	U-19Pu-10Zr	2.4%	1.84%
A814	U-19Pu-14Zr	1.6%	1.83%

3.3 Dimensional Inspection

Dimensional inspections of the three pins were performed using the HFEF contact profilometer. Outside diameter measurements were collected following the wire wrap (spiral profilometry for A797, A812) and all along the pin for A814 in roughly 0.127 cm increments and at 6 angles spaced 30 degrees apart. Diameter measurements are collected with ±0.0005 cm accuracy. It is possible to ascertain the beginning and end of the rodlets by diameter spikes associated with the welds on the extensions and rodlet endcaps.

The cladding deformation profile for all three pins is reported in Figure 4. Diametral strain is evident and ranges between 0.7 – 0.87% (max), as reported in Table 3. Max cladding strain data collected in 1990 [7] on the same set of pins match well with the data from this work. There is no apparent relation between Zr content and cladding strain when comparing the three pins and the two set of data. On the other hand, these results are well in line with the literature on D9 cladding as reported in [8].

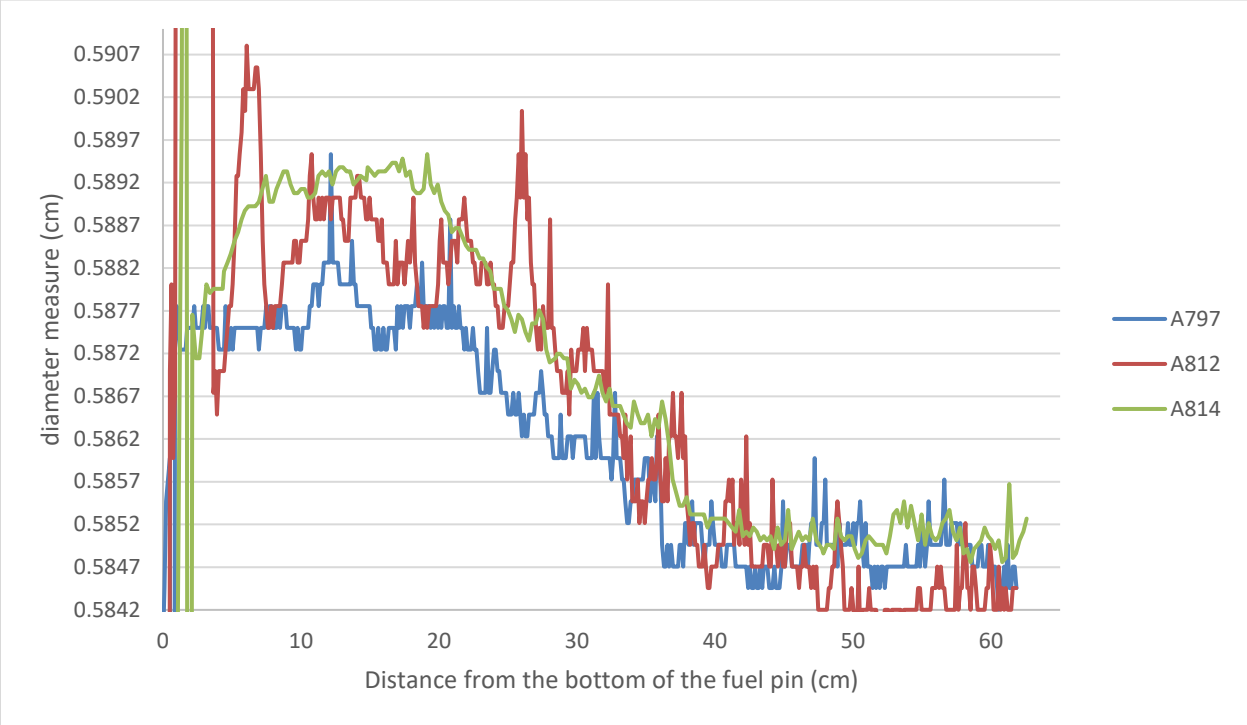

Figure 4. Cladding deformation profile for three X441A pins measured with contact profilometry.

Table 3. Max cladding strain measured with contact profilometry and comparison with historical data [7]

X441A fuel pin	Composition	Max Clad strain	Max Clad strain (old data)
A797	U-19Pu-6Zr	0.70%	0.70%
A812	U-19Pu-10Zr	0.82%	0.87%
A814	U-19Pu-14Zr	0.87%	0.87%

3.4 Gamma spectrometry

Gamma spectrometry of all X441A pins selected was performed using the HFEF Precision Gamma Scanner (PGS). The plenum portion of the pin was scanned in 0.254 cm steps, and the fueled section of each pin was scanned in 0.127 cm steps for a live time of 30 minutes.

The time elapsed from end of irradiation to PIE (more than 20 years) was so great that the only detectable isotopes were relatively long-lived radionuclides Cs-137, Eu-154, and Co-60. Figure 6 reports the Cs-137 and Eu-154 spectra for the three X441A pins.

In metallic fuel, Cs isotopes produced by fission are often dissolved in the Na bond between the fuel and the cladding. The Cs migrates with the Na above the fuel column producing a Cs activity spike above the fuel, as it can be seen clearly for all the three pins in Figure 5. The Cs-137 signal “undulation” along the fuel stuck cannot be readily related to any potential features visible from the neutron radiography (e.g., cracks, change in density, etc.).

The presence of Cs in the sodium plug (as shown in Figure 2 for X441A pins) above the fuel has historically been a good indication of pin integrity (since the pressurized gas plenum typically forces this sodium/cesium out of the fuel pin through any cladding breach in the fuel region). In these three pins the Cs-Na plugs present different formations and features, and it is possible to correlate them with the different peaks that are present in the Cs spectra as shown in Figure 6.

Europium-154 activity is presented in trace and shown in Figure 5. Eu-154 seems to migrate at both extremities of the pin into the sodium plug and in the colder region close to the end plug. This behavior is not well understood, and more studies are needed to confirm this phenomenon.

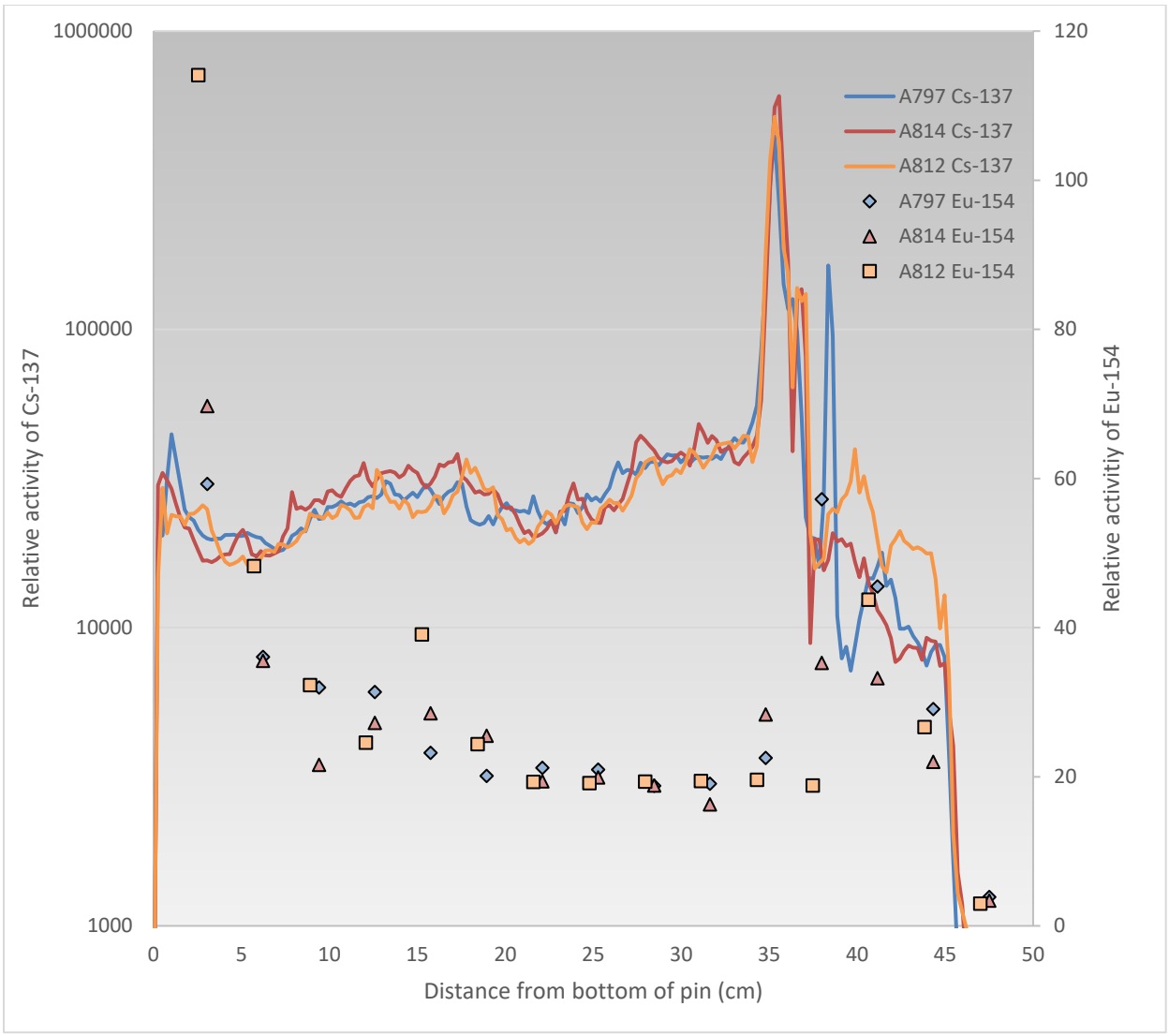

Figure 5. Gamma spectrometry of Cs-137 and Eu-154 for three X441A pins.

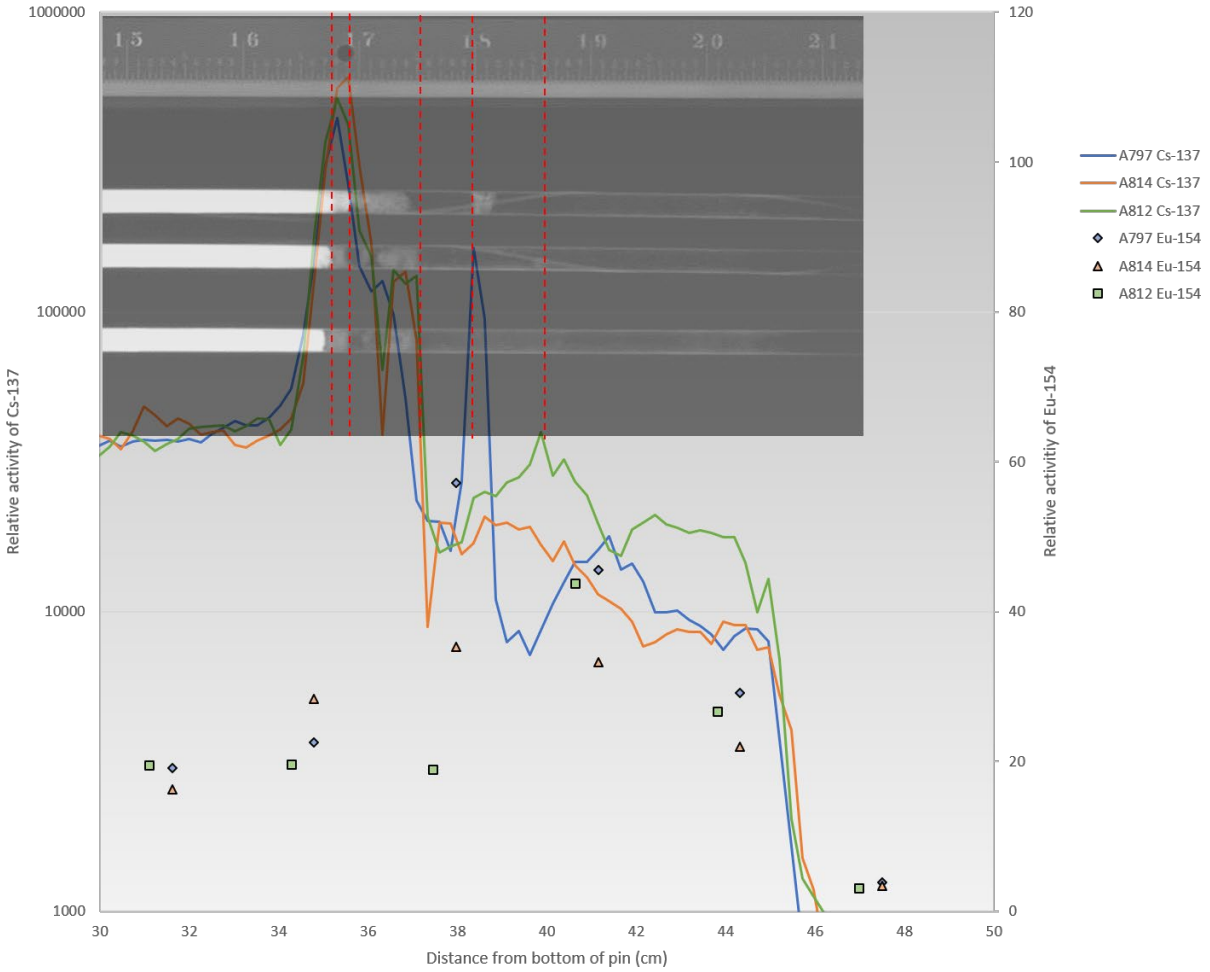

Figure 6. Cs-137 gamma spectroscopy profiles on the top of the fuel pins with superimposed the neutron radiography. The different Cs-137 peaks can be correlated with the different features on the sodium plugs.

In addition to axial gamma spectrometry scans, it is possible to rotate the HFEF PGS collimator from a horizontal to a vertical orientation. In this orientation it is possible to move an axial level of the fuel past the collimator and perform a series of rotations over several angles. The resulting signals over several angles can be collected and tomographically reconstructed to provide a two-dimensional distribution of fission products averaged over an axial location. This is referred to as Gamma Emission Computed Tomography (GECT). The full details of this technique are available in Reference [9] and the demonstration of this technique can be seen in References [10] and [11]. This technique is similar to conventional X-ray computed tomography, but it is limited by the number of angles that can practicably be collected as spectrum collected takes several minutes and the total collection time can extend to several days or weeks for a fully characterized rodlet.

The GECT technique was applied to A812 in collecting Cs-137 signal in 0.0254 cm steps over 4 equally spaced angles between 0 and 180 degrees at two different heights x/L=0.75, 0.90 from the bottom of the fuel stack. Figure 7 presents the 2D tomography reconstruction in which the distribution of Cs-137 at 0.75 (left image) is apparently quite uniform on the cross-section with perhaps some lower signal in a middle region. On the other hand, the distribution at 0.9 (right image) is slightly distorted and not symmetric.

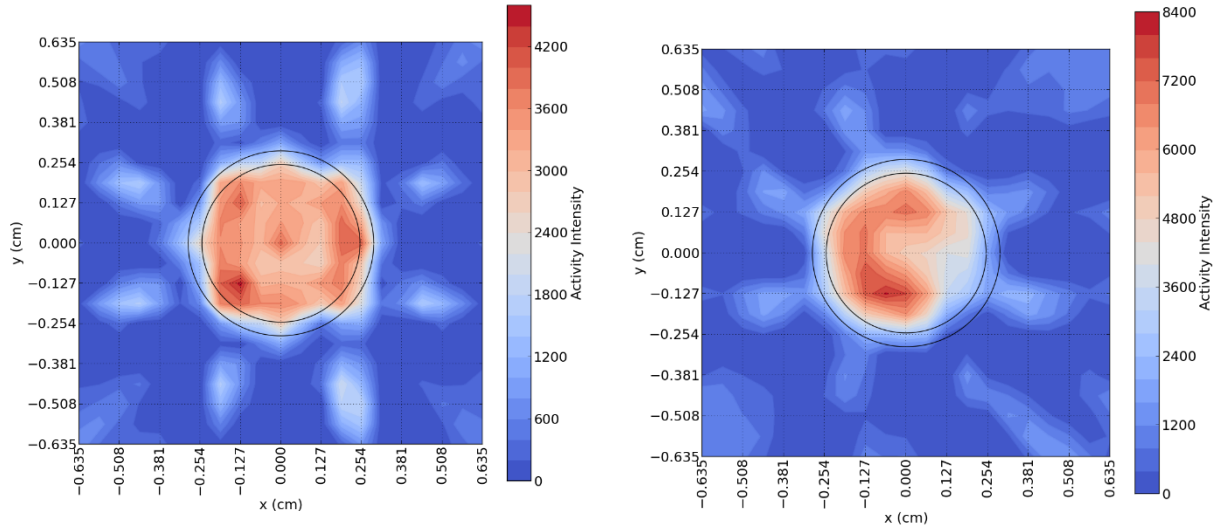

Figure 7. Tomography reconstruction of Cs-137 signal for A812-X441A at two different heights, x/L=0.75 (left) and 0.90 (right) from the bottom of the fuel stack.

4. DESTRUCTIVE EXAMINATION

Destructive examination includes fission gas release analysis, pins sectioning, chemistry / burnup analysis and metallography.

4.1 Fission Gas Release

Fission gases were collected from the fuel pins using the HFEF Gas Assay, Sample, and Recharge (GASR) system. The fuel pins were punctured using a 150 W Nd-YAG laser system, and a gas sample was collected in a stainless-steel bottle external to the hot cell for each pin. Void volume in the pin was then determined by a series of backfills into the punctured pin and expansions into the GASR system. The fuel pin internal gas pressure was derived from the void volume measurement and the initial gas pressure measurement upon puncture. Fission gas analysis was performed by gas mass spectrometry. Results of fission gas analysis provided total elemental composition, krypton isotopic composition, and xenon isotopic composition. A summary of results (Kr+Xe % release) for the three pins is shown in Table 4. The combined Kr and Xe release is based on an estimate of the number of fissions that occurred in each pin from U-235, Pu-239, and other nuclei that is input into an empirical relationship between fission and atoms of Xe and Kr produced. The number of fissions in each fuel pin was estimated from the calculated burnup reported in literature or report [1] since the burnup / chemistry analysis has not yet been performed.

The resulting fission gas releases for all three pins are in good agreement with historical norms. The metallic fuel fission gas release is close to 70 ± 10% fission gas release that is typical of 75% smeared density U-Pu-Zr fuel behavior beyond approximately 5 atom % burnup [8].

Table 4. Fission Gas Release data measured for the 3 X441A pins.

X441A fuel pin	Kr+Xe Gas Release (%)
A797	79%
A812	76%
A814	75%

4.2 Fuel pins sectioning

After performing GASR as described in the previous section, the different fuel pins were sectioned through the fuel zone at different axial positions to investigate the evolution of microstructure with the axial and radial temperature distribution as well as potential change with burnup. Radial and longitudinal cross-sections about 6 mm (radial) and 10 mm (longitudinal) in length were cut, mounted in epoxy, and polished to a 0.25 µm finish.

Additional samples were taken from different axial positions along the fuel stack (five samples for each pin) and sent to the INL Analytical Laboratory (AL) for a variety of chemical and radiological analyses and with the primary goal of burnup determination as described in subsection 4.3.

The cutting plan for the three X441A fuel pins is identical and shown in Figure 8 along with the different positions of the different samples for microscopy or burnup analysis ("AL") as described in the colored code legend. Furthermore, in Figure 8 there is also the schematic representation of the two different sample configurations for microscopy, "green" transversal mount, "blue" longitudinal.

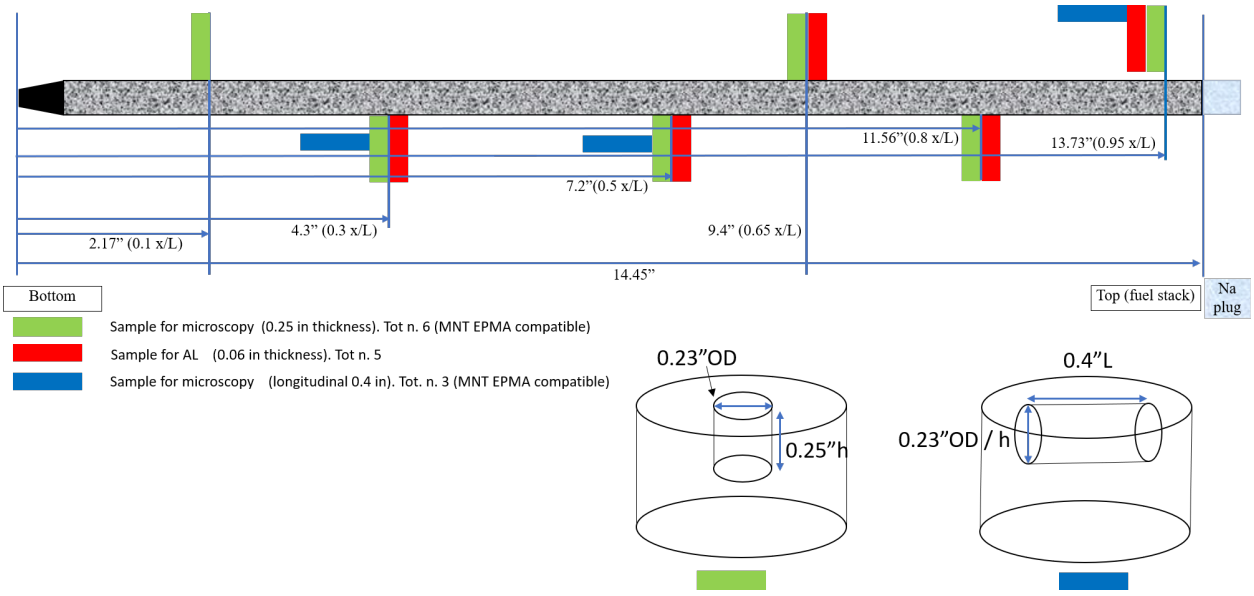

Figure 8. X441A fuel pin cutting diagram describing the different sample configuration and purpose, as well as the different axial positions.

Furthermore, a schematic representation of the two different sample configurations is reported in the drawings.

4.3 Burnup chemistry

During pin sectioning, five samples for each X441A fuel pin were taken from different axial positions along the fuel stack and sent to the INL AL for a variety of chemical and radiological analyses. The primary goal of the analysis was to ascertain the burnup of the sampled materials. Gamma spectrometry analysis was also performed.

Burnup was calculated from the results of mass spectrometry examinations of dissolved fuel samples. Samples were placed in a heated acid solution until both the fuel alloy or compound and the cladding had dissolved. Care was taken to ensure complete dissolution of all constituents which can take up to 24 hours to complete. More details on the dissolution process of similar fuel samples can be found in [12].

The determination of burnup was performed using the measured mass of a specific fission product in the fuel, the cumulative fission yield of that specific fission product, and the total mass of actinides present in the sample. This method is sometimes referred to as the "Fission Product Monitor Residual Heavy Atom" technique [13,14]. Burnup is calculated in % fission per initial heavy metal atoms (FIMA), which is comparable to heavy metal depletion and atom % burnup units used in other sources. The calculation follows the equation

$$BU = \frac{\left(N_{fp} / y_{fp} \right)}{\left(\left(N_{fp} / y_{fp} \right) + N_{Act} \right)} \times 100 \quad (1)$$

where Nfp is the number of atoms of a specific fission product (fp) measured in the sample, yfp is the cumulative fission yield of fission product fp, and NAct is the number of atoms of actinides in the sample. All fission yields were taken from ENDF/B-VII.1 [15]. A benefit of this burnup technique is that it requires no a prior knowledge of the sample. All the factors in Equation (1) can be directly measured from mass spectrometry results, and no assumptions about the pre-irradiation state of the fuel or the size of the sampled material need to be made. For this burnup analysis, the fast fission yields were used in the calculation of burnup. The burnup would be biased if only the Pu-239 cumulative fast fission yields were used in Equation (1) for burnup determination. In order to estimate the fraction of fission that occurred in a particular isotope, the effective fission yield for several isotopes was assumed to be a weighted average between the yields for U-235 and Pu-239. The weighted average for each sample was determined by finding the weights that minimized the burnup spread among the six key fission product burnup indicators for this technique (La-139, Ce-140, Ce-142, Pr-141, Nd-145, and Nd-146).

These isotopes occur on the higher atomic number peak of the bimodal fission product distribution. They are all lanthanides that will readily dissolve in the selected acid. The differences between fission yields are fairly small for these isotopes as well. All these isotopes are nonradioactive and have a relatively small neutron absorption cross section, with the exception of Nd 145. Because of its cross section, the number of Nd-145 and Nd-146 atoms in the samples and their respective yields are summed in the calculation of burnup. In this calculation, the burnup measurement for each sample of particles was found by taking the average of the individual isotope results from Equation (1) for La-139, Ce-140, Ce-142, Pr-141, and the Nd-145 + Nd-146 combined result. The uncertainty of all mass spectrometry values is ±5% (2 sigma), and the derived burnup values are also considered no better than 5% relative uncertainty.

The measured averaged fission density and burnup values and the averaged simulated burnups for the different X441A pins are shown in Table 5. The values are averaged on the different fuel samples (n. 5) analyzed along the fuel height for each fuel pin. It can be noticed that for A797 and A814 the measured and simulated burnups agree fairly well, while for A812 the values are of 1 %FIMA. The reason for this incongruency is not known at this time and a more detailed analysis into the chemistry data is needed.

Figure 9 presents an example of axial distribution of burnup for A797 pins; the peak burnup is found at around 0.4 elevation from the bottom of the fuel pin and decreases by 30% at the top of the fuel pin. This trend is well in line with the typical predicted burnup profile (shown by the light and dark blue trend curve in Figure 9) for a generic fuel pin irradiated in EBR-II as reported in [16].

Table 5. Measured averaged fission density and burnup values for the 3 X441A pins. Table reports also the averaged burnup simulated for comparison.

X441A fuel pin	Composition	Av. fission density measured (fiss/cc)	Av. burnup measured (%FIMA)	Av. burnup simulated* (%FIMA)
A797	U-19Pu-6Zr	3.36E+21	9.06%	9%
A812	U-19Pu-10Zr	4.27E+21	11.35%	10.34%
A814	U-19Pu-14Zr	3.70E+21	11.36%	11.53%
*From EBR-II IMIS database				

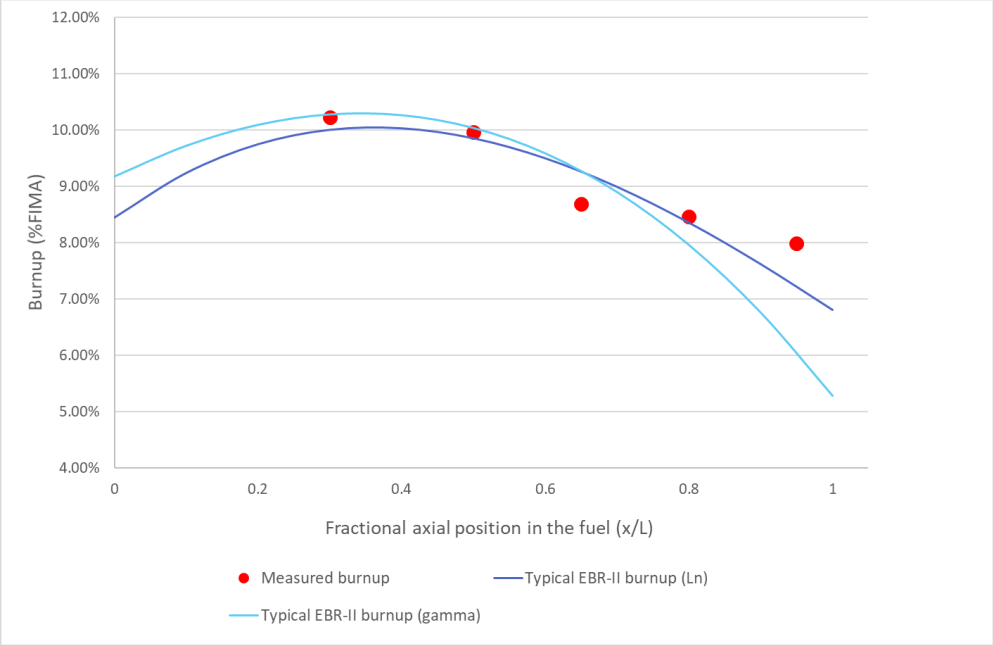

Figure 9. X441A-A797 measured axial burnup distribution. The typical EBR-II burnup profile (axial gamma activity profile for activation products in the cladding and lanthanides in the fuel) is reported for comparison [16].

4.4 Metallography

Optical microscopy was performed on a Leica DMi8 inverted microscope at INL HFEF using different magnification lenses to be able to resolve the different microstructure at different degrees of details.

Restructuring process, indicated by various microstructure morphologies exhibiting different phase compositions, has been observed along the irradiated metallic fuel radius and studied extensively [3,4,17,18]. Restructuring is strongly dependent on the irradiation temperature and is driven by changes in Zr solubility and mobility in different phases of the U-Pu-Zr ternary system [19]. Relevant background on this complex ternary can be found and summarized in Reference [20] and may aide in the interpretation of

the following microstructure in the different fuel pins. When the fuel central temperature is higher than approximately 650°C, for an alloy U-19Pu-10Zr, a bcc γ phase is formed, and the cross section of the fuel pin exhibits a 3-ring structure [3,4,17]. An example of this condition is reported in Reference [19] and Reference [11]. Very large fission gas bubbles are present in the center region, characteristic of the high temperature phase (γ-phase).The intermediate radius region is characterized by a dense phase, considered to be ζ-phase [4,21] and, in the periphery, a non-spherical porosity phase and a second phase are present, inferred to be rich in lanthanides precipitates. If the temperature condition to form γ phase is not met (fuel center temperature below 650°C), a 2-ring structure is normally observed [3,4] where the dense phase is observed in the center of the fuel cross section.

Varying the Zr content will vary the different phase transition temperatures compared to U-19Pu-10Zr and might also change the relative size of the different regions across the fuel radius. This work is enabling a systematic study of the microstructure change with the variation of the temperature axially and radially and with Zr contents. The metallography observations are summarized below.

Figure 10 shows the transverse cross-sections taken from X441A-A812, U-19Pu-10Zr along the fuel pin height, and represents an overview of the different microstructure and an estimation of the peak irradiation temperatures and phase transition temperatures. From the bottom to the top of the fuel stack (from left to right in Figure 10), the presence of a high porosity region associated with bcc phase, as mentioned before, is evident. The microstructure seems more complex compared to the usual 3-ring structure described above, having four major regions microstructure clearly visible from the different coloration.

In Figure 11 a high magnification image from X441-A814 (U-19Pu-14Zr) shows in greater details the different regions in which various degrees of porosity (in shape and orientation) are visible.

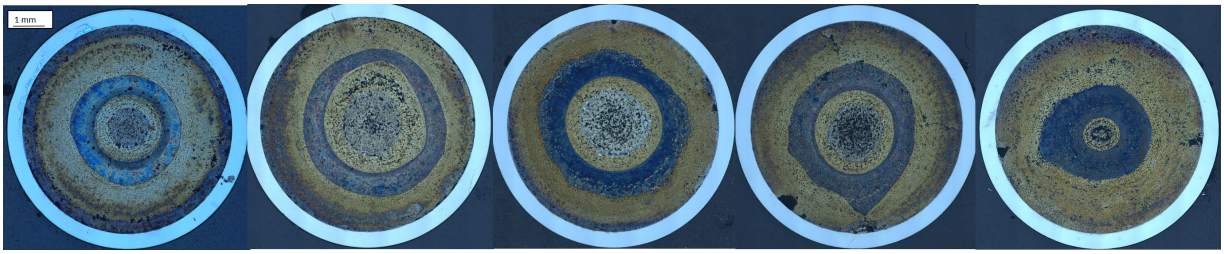

Figure 10. Optical metallography cross sections from X441A-A812, U-19Pu-10Zr, taken from different axial positions, from left to right: x/L=0.3, 0.5, 0.65, 0.8, 0.95.

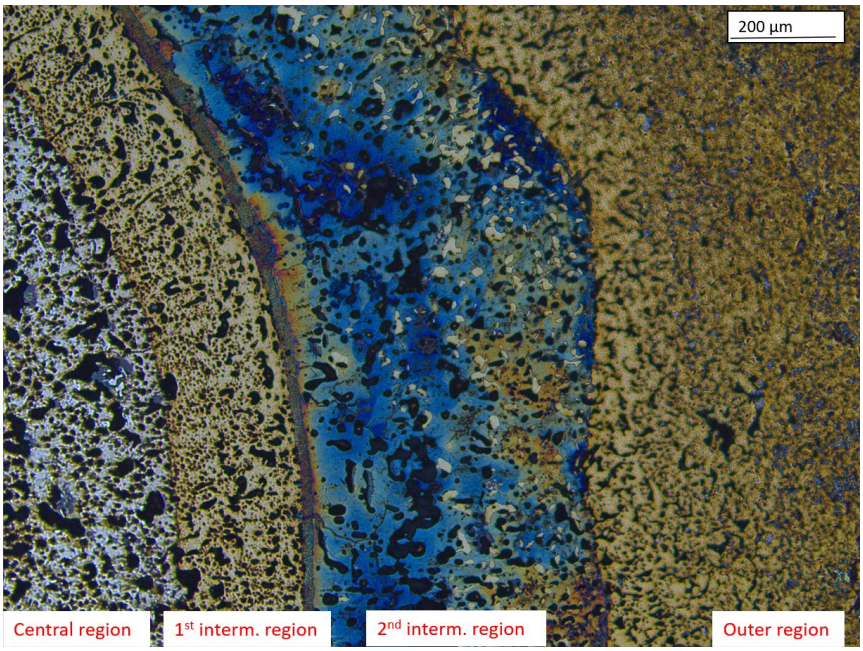

Figure 11. High magnification optical microscopy of X441A-A814, U-19Pu-14Zr, taken at x/L=0.65 in which the four regions are highlighted.

Finally, in Figure 12 it is possible to observe the comparison between the different metallography performed on the three different fuel pins at the same axial height. As was already discussed in Reference [1] the fuel restructuring is only marginally affected by the Zr content. As the Zr content is varied, the sizes of the inner and middle zones change: the size of the high-Zr (bcc phase) central zone increases with the Zirconium content while the thickness of the low-Zr middle zone (inferred here to be the colored blue) decreases with the Zirconium content. The size of the outer zone is approximately the same for all three Zr-variable fuel types.

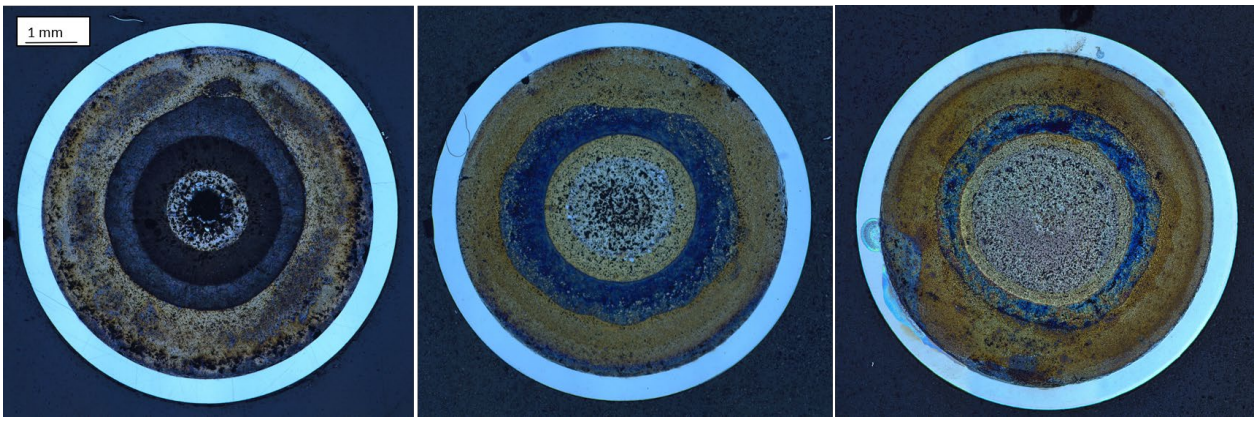

a) b) c)

Figure 12. Metallography comparison of three fuel samples taken from each X441A fuel pin at x/L=0.65. a) A797, U-19Pu-6Zr; b) A812, U-19Pu-10Zr; c) A814, U-19Pu-14Zr.

5. ELECTRON MICROSCOPY CHARACTERIZATION

Electron microscopy characterization techniques such as scanning electron microscopy (SEM), electron probe micro analyzer (EPMA), and focus ion beam / transmission electron microscopy (FIB/TEM) are applied on selected fuel samples representative of the three selected X441A pins.

5.1 Scanning Electron Microscopy

Only a limited amount of electron microscopy has been performed on irradiated metallic fuels historically. The dose rates from full cross sections of irradiated fuels are typically too high for sample handling and loading into electron microscopes that are typically operated in unshielded radiological facilities. The dose rates often cause issues with the electronics in electron microscopes and their associated detectors.

In recent years it was possible to place some metallic fuel samples [12,22,23] in the SEM at the INL Electron Microscopy Laboratory (EML). Thanks to state-of-art SEM instrumentation, it is possible to conduct a throughout microstructure characterization of irradiated metallic fuels. This instrumentation is also helpfulin down selecting interesting sites for TEM analysis. Also, the SEM is equipped with energy dispersive X-ray spectroscopy (EDS) which enables the possibility of semi-quantitatively measuring the different elements and mapping larger areas.

Building up from these experiences and good practices, three metallic fuels full cross-section from X441A (each from the same axial position x/L=0.65) have been analyzed with SEM-EDS. The metallography of those three samples is reported in the previous section in Figure 12.

Back-scattered electron (BSE) imaging of the three samples montages is shown in Figure 13. In this figure, brighter areas indicate areas of higher electron density associated with higher atomic number elements. Some carbon paste or dirt remaining from sample preparation is visible in Figure 13 b, c as a dark grey homogenous feature.

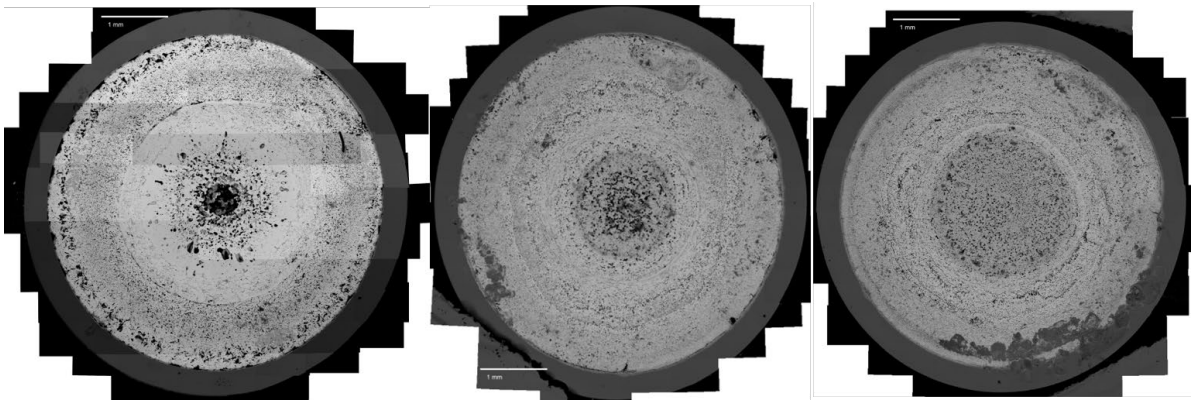

a) b) c)

Figure 13. BSE montages of the fuel samples taken from each X441A fuel pin at x/L=0.65. a) A797, U-19Pu-6Zr; b) A812, U-19Pu-10Zr; c) A814, U-19Pu-14Zr.

The same pore size distribution seen in the optical microscopy is also seen in the electron microscopy; the central microstructure is very porous and difficult to retain when the sample is prepared, thus some fuel pullout can be seen, especially from the U-19Pu-6Zr.

Figure 14 is a direct comparison between the SEM-BSE and the metallography for the U-19Pu-6Zr alloy in which the different regions are identified and highlighted. It can be noted in the metallography that the four regions are very well-defined compared to SEM, in which Region 2 and Region 3 seem more blended together at this magnification, and Region 1 in the SEM-BSE does not present any sharp

boundaries like in the optical image. Metallography seems very sensitive to any particular change in Zr content / oxidation sensitivity.

In Figure 15 the different regions from the SEM-BSE montage of Figure 14 are presented in higher magnification, and it is possible to observe in more detail how complex the microstructure of this fuel system is.

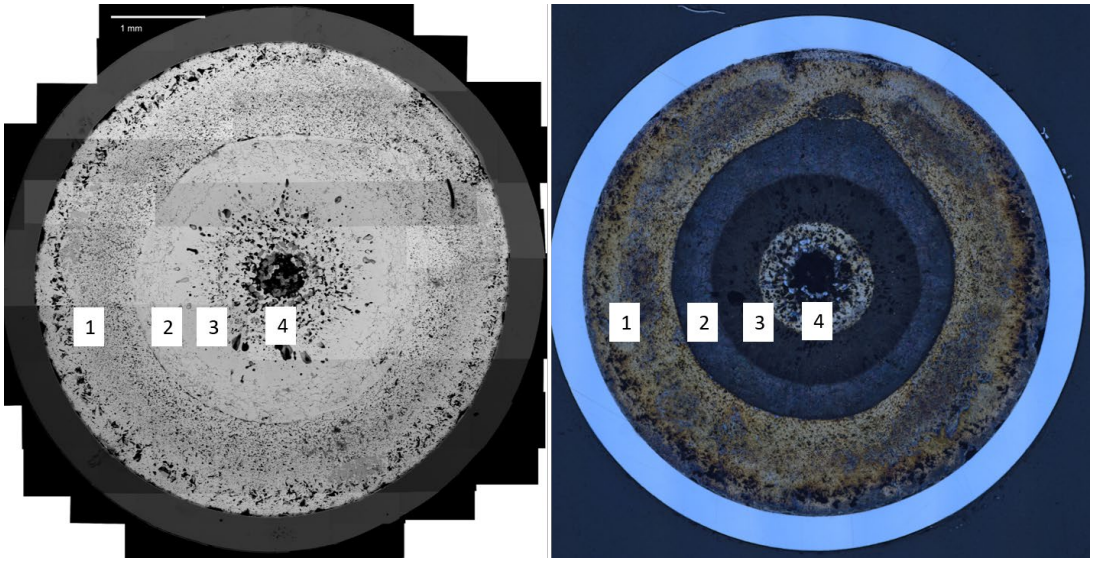

Figure 14. U-19Pu-6Zr comparison between SEM-BSE montage and metallography. The different regions are also highlighted.

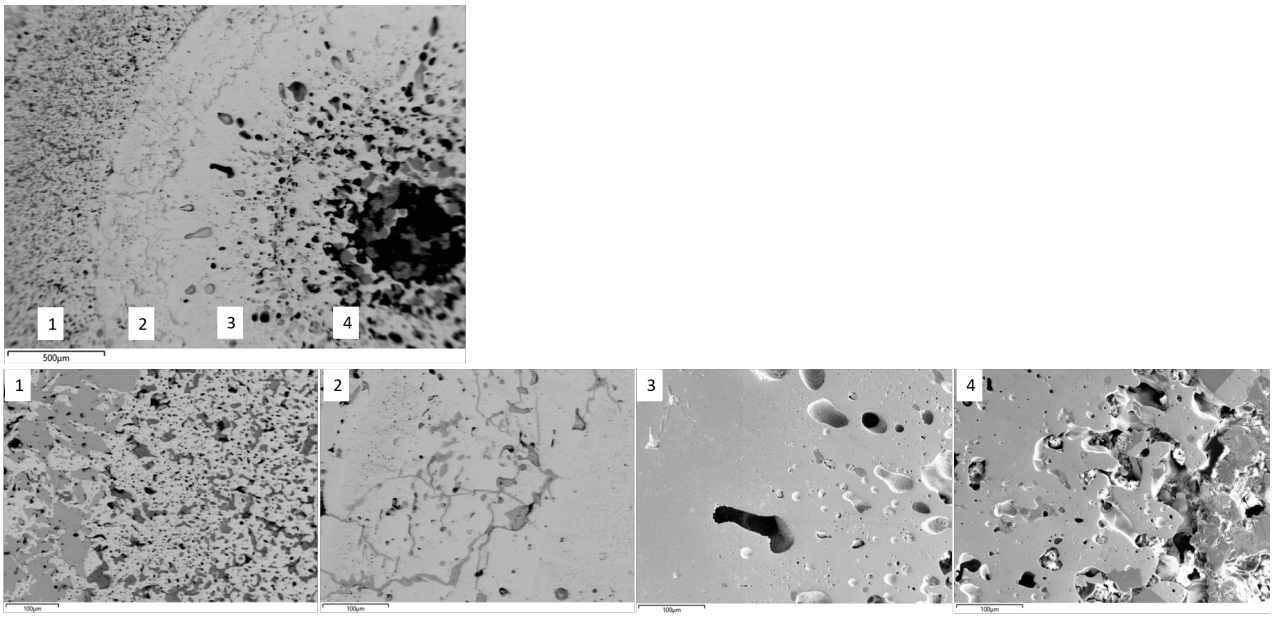

Figure 15. BSE images magnification of the different regions observed in the SEM-BSE montage from Figure 12.

The redistribution of Zr in the fuel matrix is similar to what has been reported in literature for U-20Pu-10Zr and three regions' structure [19]. High Zr concentration is present in the central region of all three fuel samples with values around 10 wt% (A797), 30 wt% (A812), 35 wt% (A814). These concentrations may suggest a possible central fuel structure of γ (U,Pu,Zr) under reactor conditions and

most likely transformed to δ (U, Pu)Zr_2 after shutdown. Depending on the local temperatures and kinetics experienced during shut down / cooling and the different phase diagrams of the fuel alloys, several different phases can be also present such as ζ (U,Pu), α(Zr), α(U). The complexity of the system can be seen in Figure 16 which shows an example of the fuel central region microstructure that differs between the different alloys. In the higher Zr contents alloys, the grain boundaries of the BCC-γ are visible with several "cooled" structures growing within. Different situations are found in the U-19Pu-6Zr in which a lamellar structure is evident.

Insights on the different phases present will be possible with the planned TEM and diffraction patterns studies.

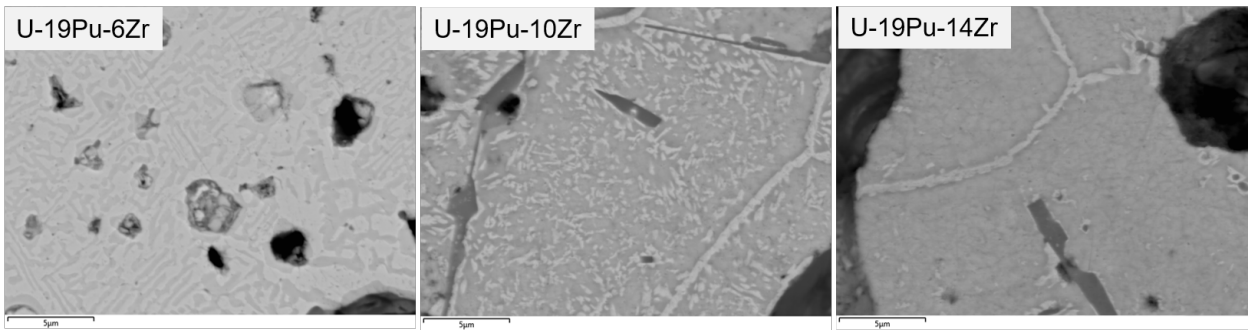

Figure 16. BSE high magnification images of the central fuel regions microstructure

Beginning approximately 50% of the way from the center of the fuel, Region 1 in Figure 15, the concentration of secondary phases and lanthanides - noble metals precipitates is higher compared to the other regions. Figure 17 reports an EDS semi-quantitative maps of the main elements present in part of Region 1 from Figure 15. It is evident the presence of a large lanthanides precipitate (Nd maps are reported as examples) with an approximate composition of Ln_7Pd_3 (Ln=Ce, Nd, La, etc.); this agrees with observations from irradiated U-10Zr [23].

Furthermore, Figure 17 also presents an example of fuel cladding chemical interaction (FCCI) region in which the attack from lanthanides into the cladding can be seen, as well as Ni and Fe behavior. For this specific fuel-cladding system in particular, Ni penetrates further into the cladding compared to Fe, as also seen in literature [24].

There is no apparent dependency from the Zr content of the development of the wastage layer into the cladding as could be expected from experience and research that would have suggested a protective nature of Zr-rind that is normally produced in fabrication. In U-19Pu-6Zr the average wastage thickness is around 8 μm compared to the 30 μm of the other two fuel pins. As already preliminary noticed in Reference [1], FCCI is most strongly influenced by the concentration of lanthanide fission products at the fuel/cladding interface rather than the bulk fuel composition or temporary and limited surface barriers (e.g., Zr-rind). Considering the semi-quantitative nature of EDS analysis, the fuel specimens were next examined using EPMA.

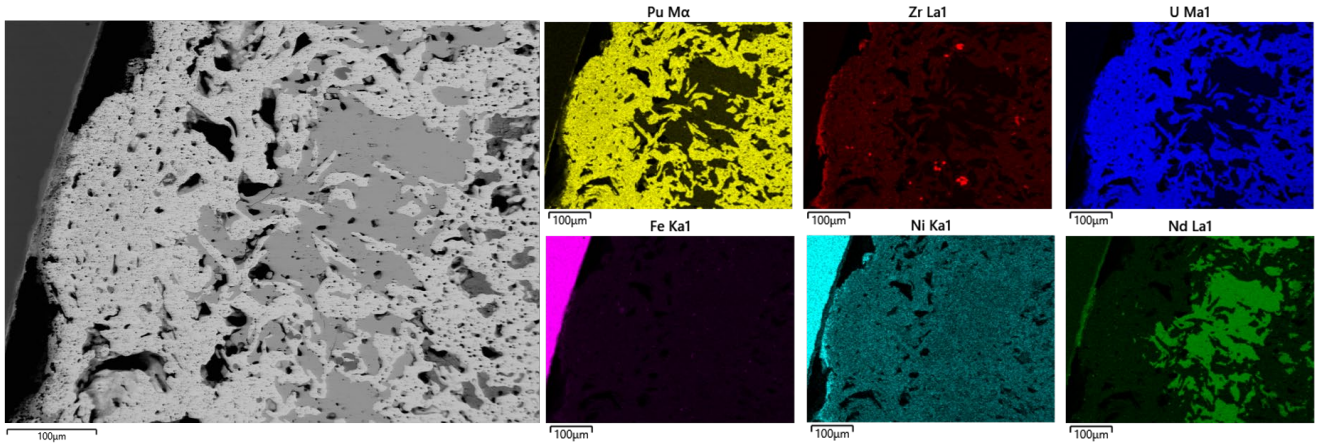

Figure 17. BSE image and EDS semi-quantitative maps of selected elements of part of Region 1 from Figure 15.

5.2 EPMA

Electron probe microanalyzer (EPMA) was performed on the same three cross-sections to conduct a fully quantitative analysis of the exact composition of the redistribution of the main elements, the different regions / phases, and FCCI zones.

The instrument used is a Cameca SX100R EPMA shielded to 3 Ci of 137 Cs. Method details are available in Wright et al [25]. Briefly, quantitative analyses were conducted with a 25 keV accelerating voltage and currents ranging from 40 to 200 nA, depending on the type of analysis. The step size employed in diameter traverses ranged from 10 to 50 µm, with attempts made to avoid porosity. Probe for EPMA (v. 12.4.6) was used to process quantitative point data while Cameca Peak Sight (v. 5.1) and Probe Image (v. 1.3.5.2115) were used for map acquisition. All X-ray data were corrected for peak overlaps, absorbance, fluorescence, and atomic number using the PAP matrix algorithm of Pouchou and Pichoir [26]. Mass absorption coefficient databases employed for actinide elements was that of Farthing and Walker [27] and for lower Z elements was that of Reference [26]. Figure 18 (a-c) shows a BSE of each pin cross section illustrating analyzed areas in each sample. The entire cross-section of the fuel was scanned in EPMA and maps were collected from regions highlighted with a yellow rectangle in Figure 16. In addition to diameter maps, localized maps were collected from the central region (shown in purple), transition regions (shown in black), FCCI regions (shown in red), and U-rich regions (shown in blue). The selection of these regions was based on the initial diameter map and SEM data discussed in section 5.1.

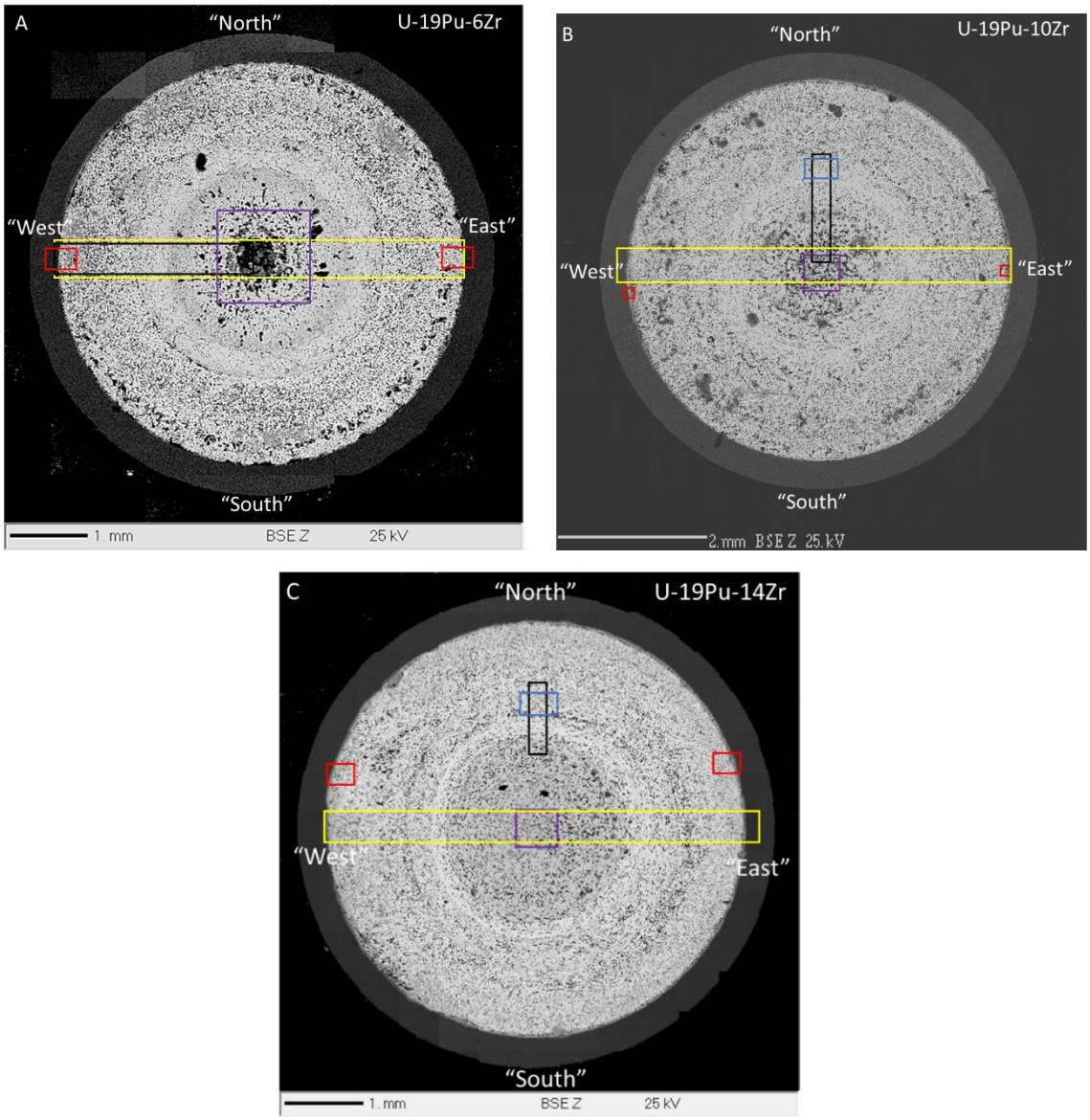

Figure 18 (a-c). Locations for regions described in the report for a) A797, U-10Pu-6Zr; b) A812, U-19Pu-10Zr; and c) A814, U-19Pu-14Zr.

Diameter maps are shown in yellow, FCCI locations are shown in red, the center zone is shown in purple, transition maps are shown in black, and high-U regions are shown in blue. Directions (e.g., "West") are shown on each image and are referred to in the text.

5.2.1 Compositional Zone Formation

Figure 19(a-c) shows BSE images of each of the examined fuel samples with identified zones outlined. These zones differ compositionally, which are shown in the images with lighter gray (higher average Z) and darker gray (lower average Z) colored zones, as was also seen in Subsection 5.1. Fives zones were tentatively identified in U-19Pu-6Zr, same as in Figure 12 but the fuel center is divided in two zones. Four zones were identified in the other two fuel samples. Fuel samples U-19Pu-10Zr and U-19Pu-14Zr held together well during polishing, but the center was plucked from U-19Pu-6Zr, leaving a lanthanide-rich hole surrounded by precipitates. Because of this sample damage to U-19Pu-6Zr sample, the U, Pu, and Zr composition in Zone 1 was impossible to determine with certainty. Because of the

uncertainty surrounding the fuel element composition in this region, it is not certain whether Zone 1 and Zone 2 should be divided into two zones or whether they comprise one zone. As Zone 1 is encircled by Zr(Ru, Rh, Pd, Mo)-like precipitates, Zone 1 and Zone 2 are tentatively identified as two separate zones.

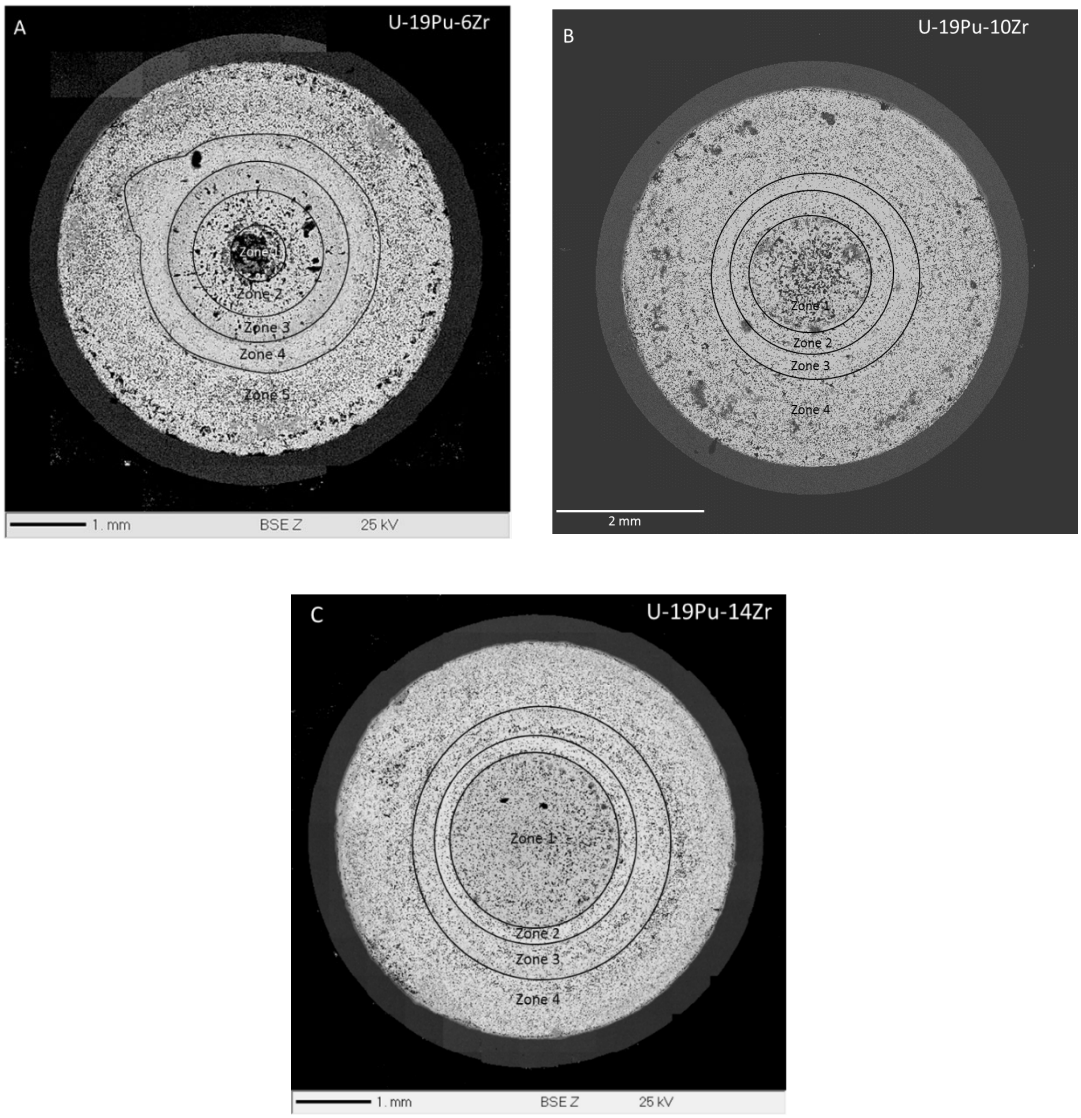

Figure 19 (a-c). Shows distinct zones for a) A797, U-10Pu-6Zr; b) A812, U-19Pu-10Zr; and c) A814, U-19Pu-14Zr.

Zone thickness varies among the three fuels (Table 6[a-c]) with the largest difference occurring in the fuel samples' respective center zones (Zone 1). The Zone 1 diameter (measured horizontally) was smallest at 630 µm for U-19Pu-6Zr and increased to 1720 µm for U-19Pu-10Zr and 2150 µm for U-19Pu-14Zr. In contrast, the outermost zone for each sample decreased in thickness from an average of 935 µm in U-19Pu-6Zr (Table 3a) to 635 µm in U-19Pu-10Zr (Table 6b), and to 437 µm in the U-19Pu-14Zr sample (Table 3c). These zones can be observed in Figure 20-22.

Table 6 (a-c). Zone thickness on both measured sides of a) U-19Pu-6Zr; b) U-19Pu-10Zr; and c) U-19Pu-14Zr.

a.

U-19Pu-6Zr	Thickness (μm) East Side	Thickness (μm) West Side
Zone 1	290	340
Zone 2	270	320
Zone 3	280	420
Zone 4	770	530
Zone 5	940	930

b.

U-19Pu-10Zr	Thickness (μm) East Side	Thickness (μm) West Side
Zone 1	780	940
Zone 2	390	310
Zone 3	620	550
Zone 4	590	780

c.

U-19Pu-14Zr	Thickness (μm) East Side	Thickness (μm) West Side
Zone 1	1130	1020
Zone 2	250	200
Zone 3	430	400
Zone 4	790	960

Figure 20(a-g) shows a BSE image of the sample, the quantitative horizontal diameter compositional profile, and quantitative diameter X-ray maps of U, Pu, Zr, Nd, and Pd for fuel sample U-19Pu-6Zr. These elements are shown as they represent many of the salient fuel behavioral features. U, Pu, and Zr maps illustrate fuel element behavior while Nd is representative of lanthanide element behavior. Pd is shown because it sometimes precipitates with lanthanide elements and may mitigate FCCI [28]. Similar figures are shown for U-19Pu-10Zr (Figure 21) and U-19Pu-14Zr (Figure 22).

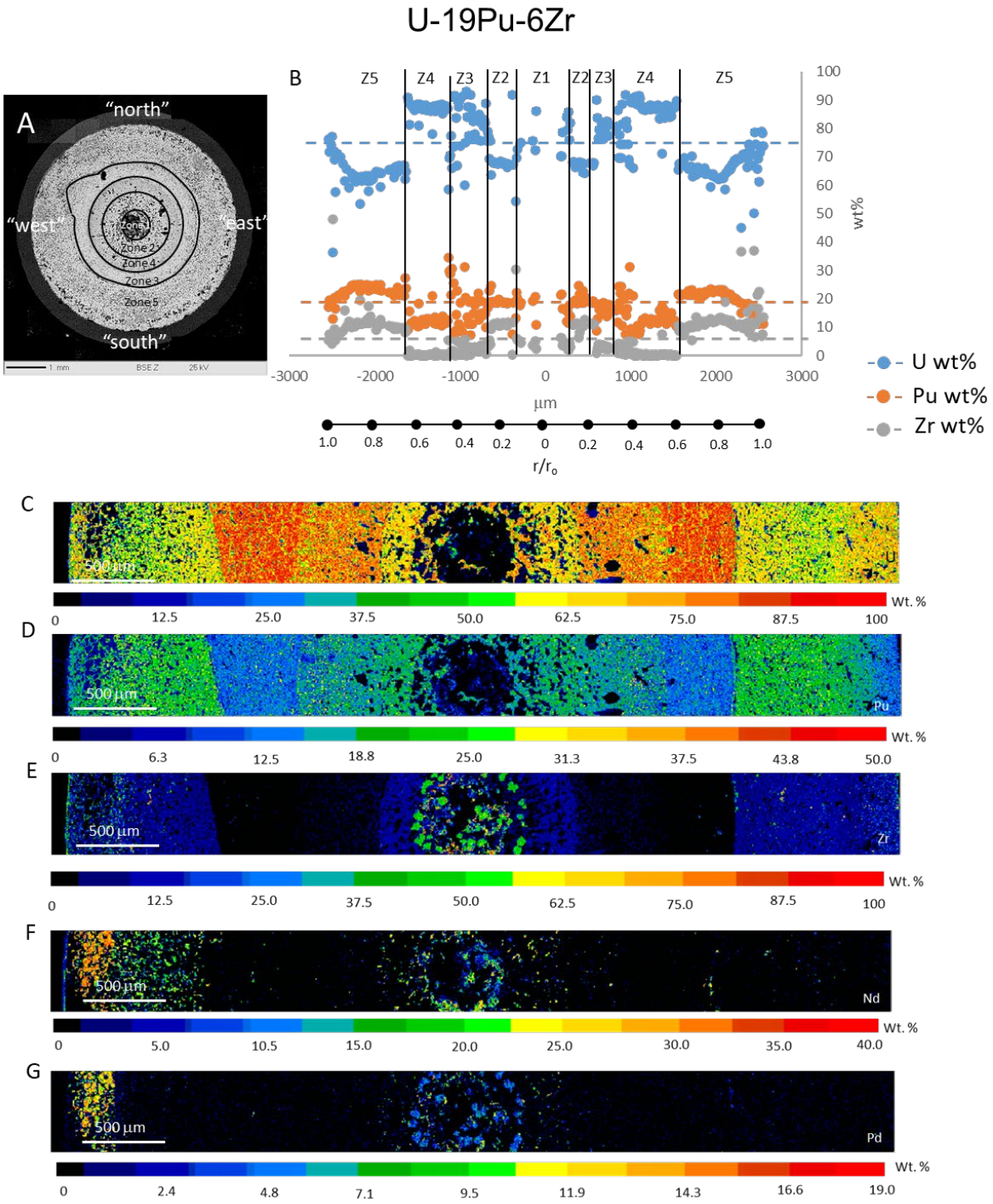

Figure 20 (a-g). a) Backscattered image of U-19Pu-6Zr with b) horizontal diameter quantitative U, Pu, and Zr traverse with zones marked, and c-g) quantitative X-ray maps of U, Pu, Zr, Pd, and Nd, respectively.

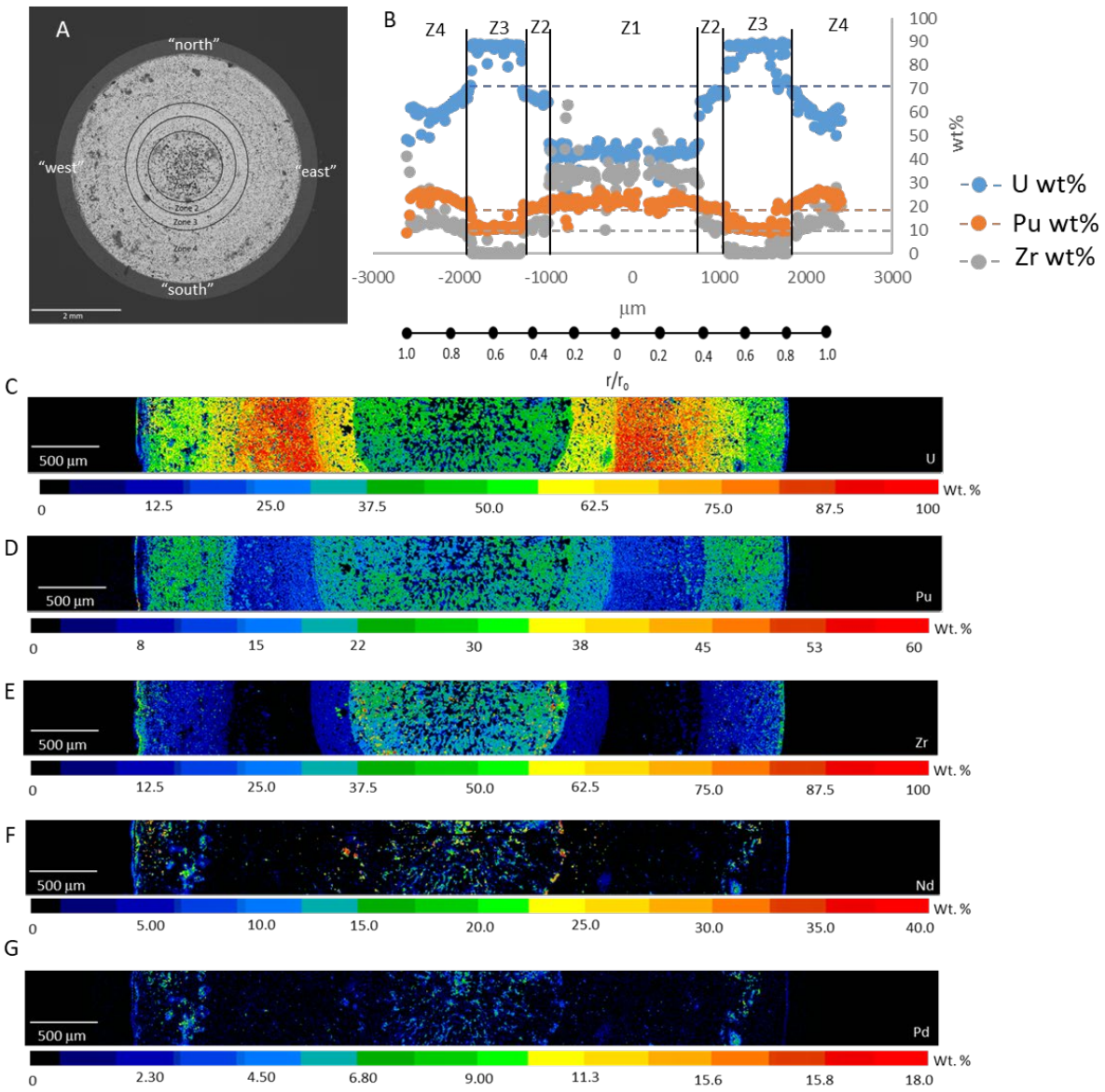

Figure 21 (a-g). a) Backscattered image of U-19Pu-10Zr with b) horizontal diameter quantitative U, Pu, and Zr traverse with zones marked, and c-g) quantitative X-ray maps of U, Pu, Zr, Pd, and Nd, respectively.

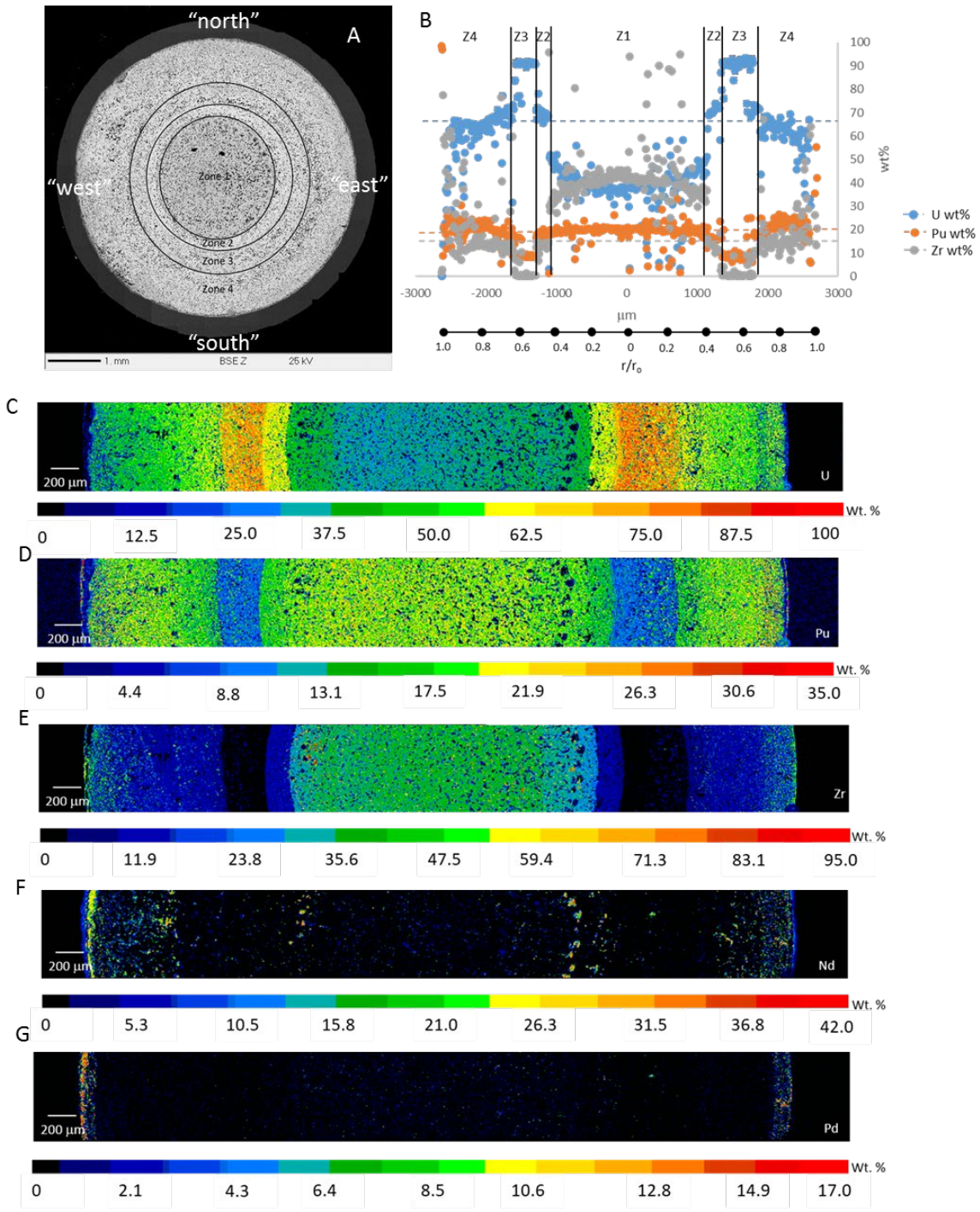

Figure 22 (a-g). a) Backscattered image of U-19Pu-14Zr with b) horizontal diameter quantitative U, Pu, and Zr traverse with zones marked, and c-g) quantitative X-ray maps of U, Pu, Zr, Pd, and Nd, respectively.

If outlier points are excluded (points that likely represent secondary phases or large pores), the U compositional range across the diameter of each sample is approximately 60-90 wt% for U-19Pu-6Zr, 40-90 wt% for U-19Pu-10Zr and 35-90 wt% for U-19Pu-14Zr. Zr concentration profiles are contrary to U concentration profiles (i.e., they move in opposite directions). For U-19Pu-6Zr, Zr ranges from approximately 0.1-14 wt%. For U-19Pu-10Zr and U-19Pu-14Zr, Zr concentrations range from approximately 0.1-38 wt% and 0.2-42 wt.%, respectively. Pu concentrations are similar for all three samples and range from approximately 6-26 wt%. U-19Pu-14Zr shows the largest compositional range for U and Zr while U-19Pu-6Zr shows the smallest compositional range. This is seen most clearly with Figure 18b, Figure 19b, and Figure 20b.

Each sample contains a zone with approximately 90 wt% U (Figure 3c, Figure 4c, Figure 5c), which increases in thickness with increasing pre-irradiation U fuel content. The average Pu content within this zone increases with decreasing Zr content. In the high-U zone of the U-19Pu-14Zr sample, abundant Pu- and Mo-rich phases form while in the similar zone in the U-19Pu-10Zr sample these phases are small and very sparse. No high Pu phases were observed in the high-U zone in sample U-19Pu-6Zr.

In all three samples, two FCCI regions on opposite sides of each sample were examined. FCCI is not symmetrical about the pins' circumference as can be observed by examining Nd and Pd behavior at the cladding interface in Figure 18 (f, g), Figure 19 (f, g), and Figure 20 (f, g). For each sample, the Nd and Pd accumulation near the cladding is much more pronounced on one side compared to the opposite side.

5.2.2 Fuel pin center

Figure 21 through Figure 23 show Zone 1 and Zone 2 in U-19Pu-6Zr and a portion of Zone 1 in the other two examined samples. U-19Pu-6Zr and U-19Pu-10Zr both show elongate pores that group together to form a rough circle about the sample center (Figure 21a and Figure 22a), whereas U-19Pu-14Zr lacks that feature (Figure 23a). U-19Pu-10Zr and U-19Pu-14Zr both contain small phases with Zr contents greater than 70 wt% (Figure 22d and Figure 23d); however, U-19Pu-6Zr appears to lack these small phases. Instead, it has abundant, large (approximately 80-100 μm) equant grains that are Zr (Ru, Rh, Pd, Mo)-like in composition (Figure 21 [d-e]).

U-19Pu-14Zr shows the presence of fission products Ba, Cs, and Nd residing primarily in pores (Figure 23 e-g). While U-19Pu-10Zr and U-19Pu-6Zr also have fission products present in pores (Figure 21 [f, g]) and Figure 22 [e-g]), they are in higher concentration and are more aerially extensive than those observed in U-19Pu-14Zr. In particular, Nd and other lanthanide elements accumulate in the pores of the lower-Zr fuels. In U-19Pu-6Zr, Nd can be observed in pores that extend radially from the center (Figure 21g). In some locations (e.g., Figure 21g and Figure 22g) lanthanide elements appear to form Ln_2O_3-like phases, although crystal structure information is necessary for positive phase identification.

Figure 24 through Figure 26 show a higher magnification view of the zones present in the examined fuel samples (note that Zone 4 is absent from Figure 26). Figure 24 shows the abrupt compositional changes that occur at zone boundaries. For example, in Figure 24b the uranium concentration in Zone 2 is approximately 68 wt%. In Zone 3 it increases to approximately 75 wt% and reaches its maximum of approximately 87 wt% in Zone 4. Zone 5 U concentrations are around 65 wt%. Zr behaves in the opposite manner (Figure 24d). Pu compositional changes are more muted (Figure 24c). Nd and other lanthanide elements are nearly absent from Zone 3 and Zone 4, but become abundant in the outer part of Zone 5 as it approaches the cladding (Figure 24g). Note that Nd co-occurs with Pd and Rh near the cladding but does not tend to co-occur with these elements throughout the remainder of Zone 5.

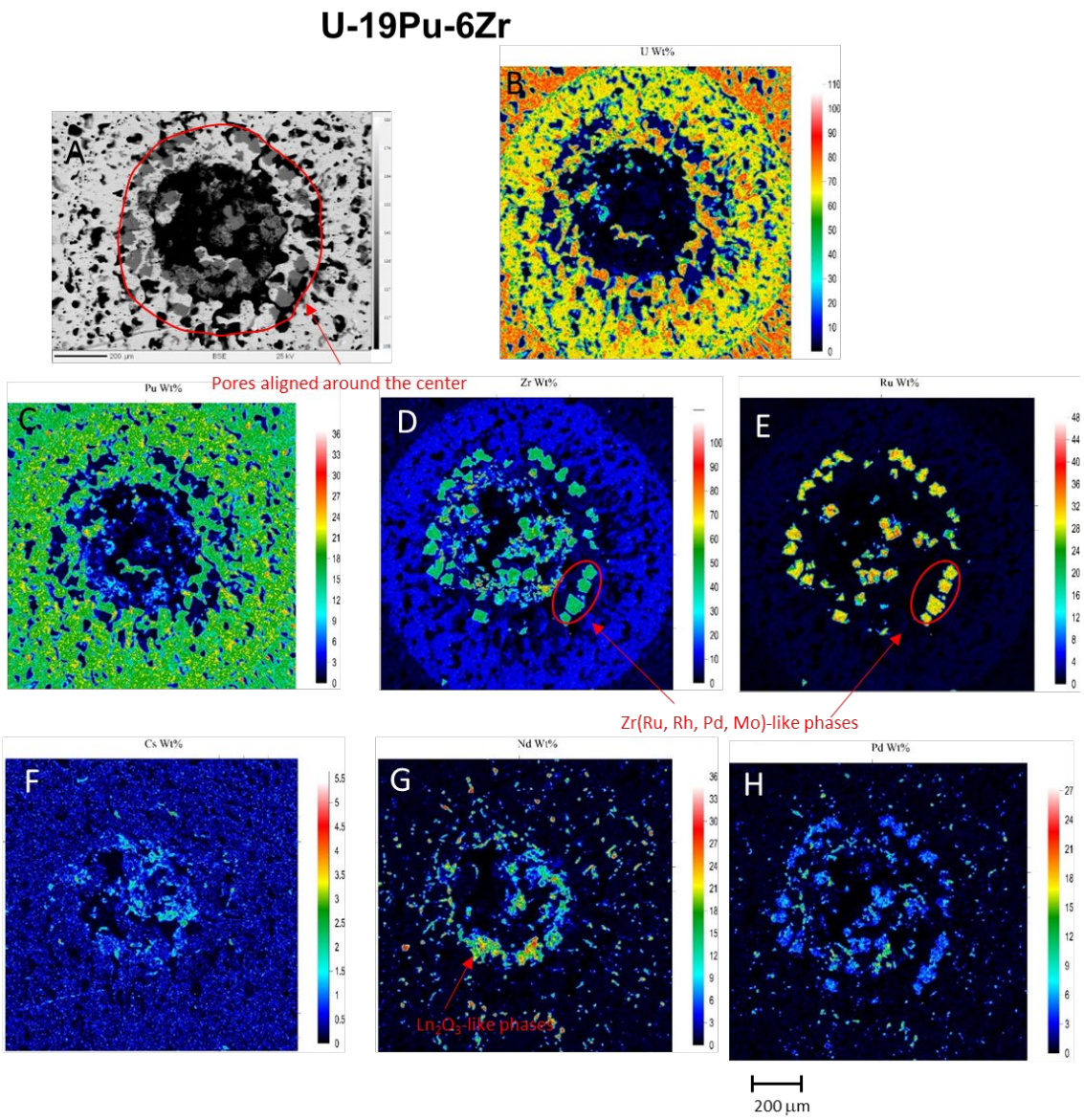

Figure 23 (a-h). a) Backscatter image of the center of U-19-6Zr; (b-h) X-ray maps of U, Pu, Zr, Ru, Cs, Nd, Pd, respectively. Mapped area is shown in Figure 18a with the purple box.

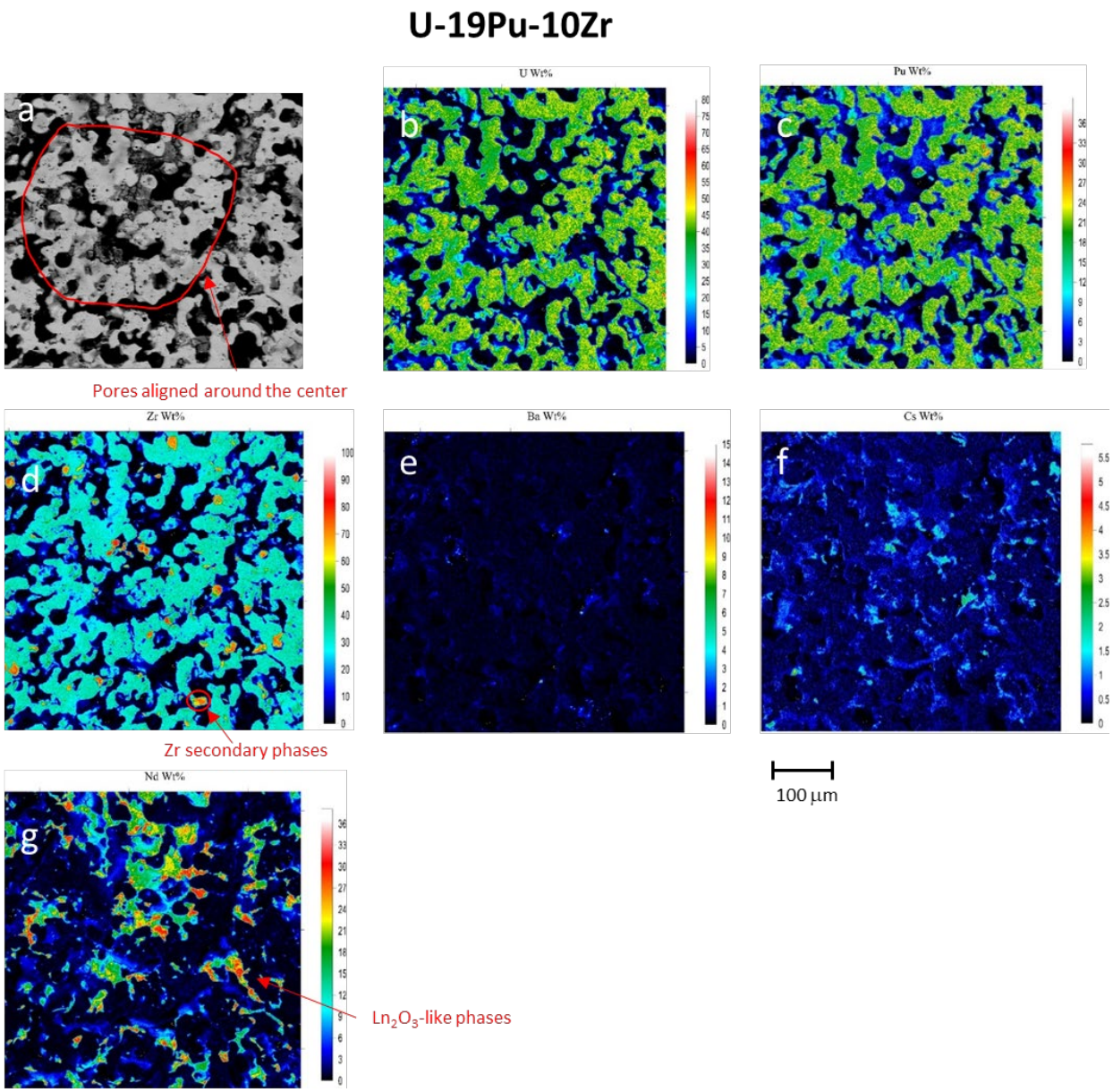

Figure 24 (a-g). a) Backscatter image of the center of U-19-10Zr; (b-h) X-ray maps of U, Pu, Zr, Ba, Cs, Nd, respectively. Mapped area is shown in Figure 18b with the purple box.

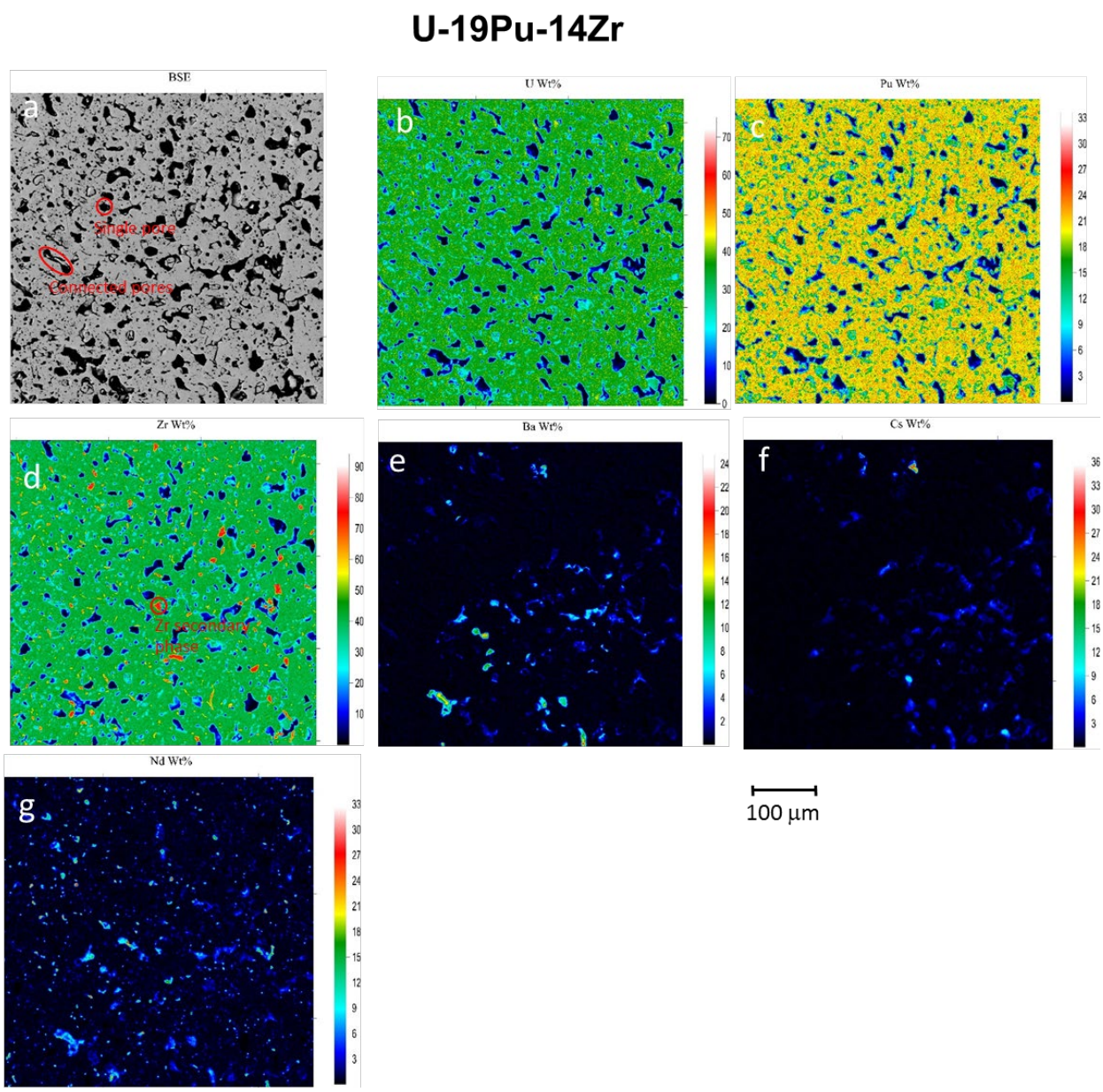

Figure 25 (a-g). a) Backscatter image of the center of U-19-14Zr; (b-h) X-ray maps of U, Pu, Zr, Ba, Cs, Nd, respectively. Mapped area is shown in Figure 18c with the purple box.

Figure 25a shows abrupt compositional changes in U-19Pu-10Zr that were observed in U-19Pu-6Zr. Figure 25 (a-d) shows that the U concentration in Zone 3 is approximately 88 wt% while the Pu, Zr, and Mo concentrations are approximately 11, less than 1, and less than 1 wt%, respectively. There are some sparsely located Pu-rich phases in Zone 3 with approximately 18 wt% Pu, 3 wt% Zr and 1 wt% Mo. Small, sparsely located elevations of Rh, Pd, and Nd (Figure 25 [e-g]) occur in all zones. Notably, the periphery of Zone 1 is quite lanthanide-rich with abundant occurrences of what are compositionally Ln_2O_3 phases (Figure 25g).

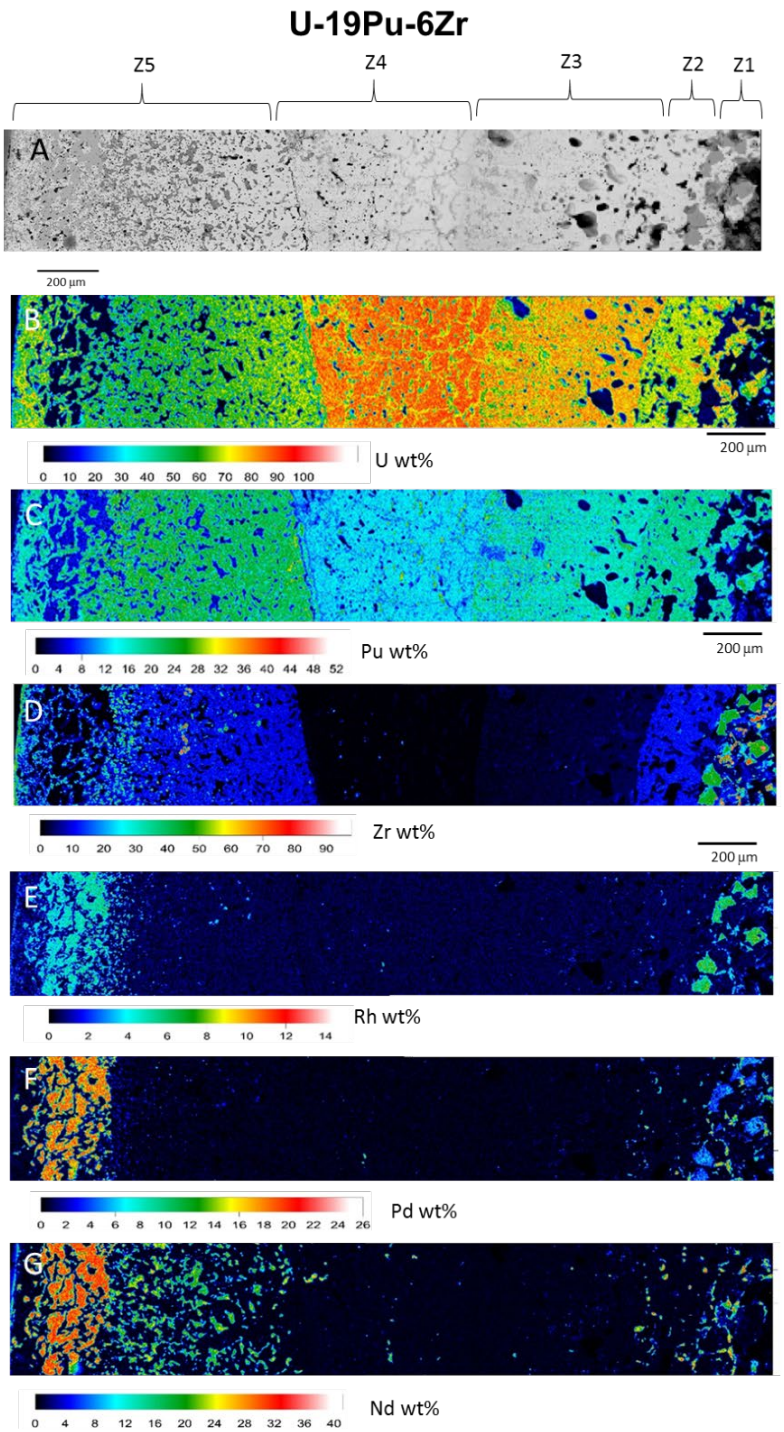

Figure 26 (a-g). a) Backscatter electron image of a radial section of U-19Pu-6Zr obtained from the west side. b-g) quantitative X-ray maps of U, Pu, Zr, Rh, Pd, Nd, respectively. Mapped area is shown in Figure 18a in the black box. Note that the fuel center is toward the right side of the images.

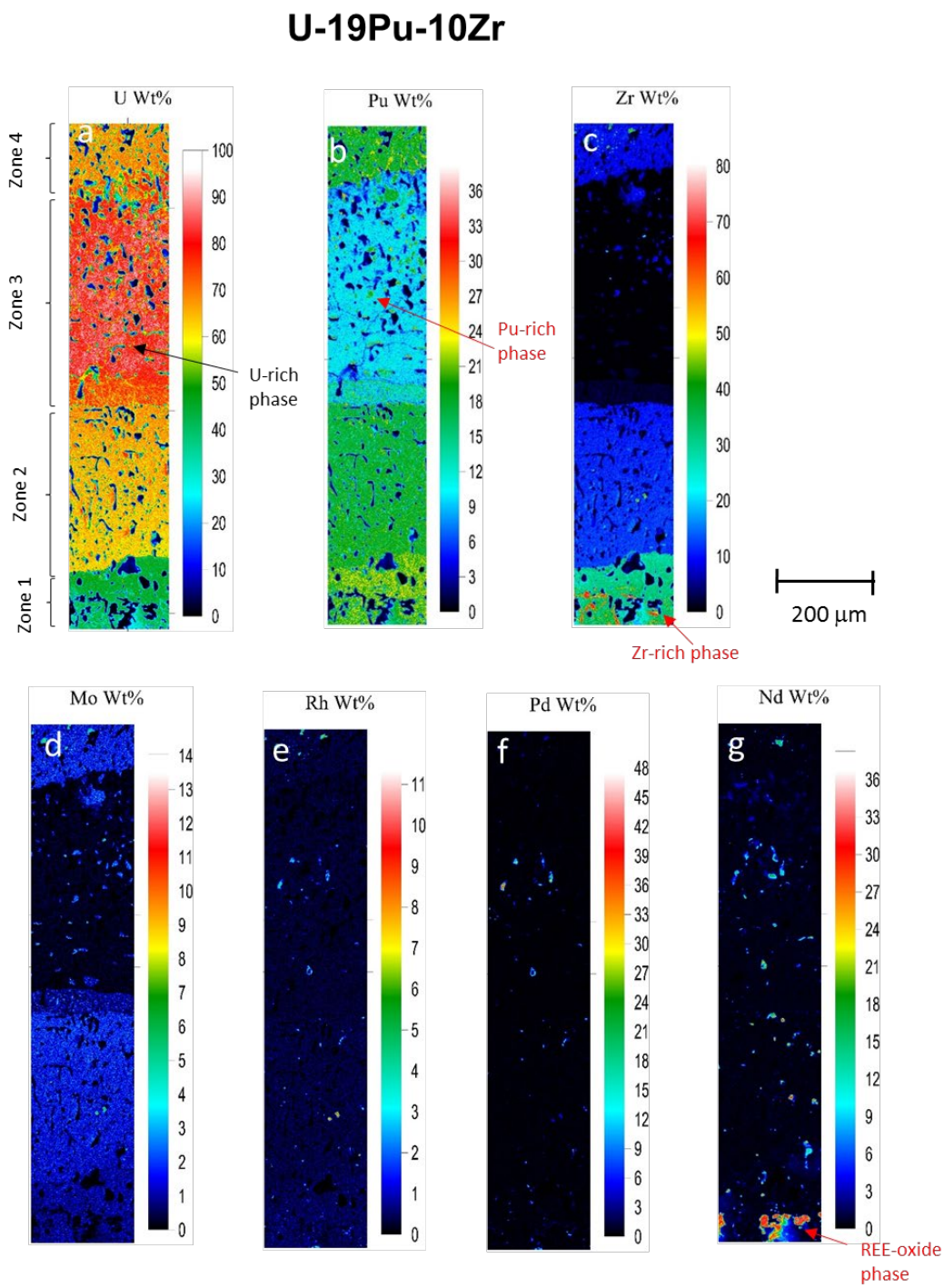

Figure 27 (a-g). a) Backscatter image of the center of U-19-10Zr; (b-g) X-ray maps of U, Pu, Zr, Mo, Rh, Pd, Nd, respectively. Mapped area is shown in Figure 18b with the black box. Note that the fuel center is toward the bottom of the images.

The compositional changes occurring in Figure 26 (a-h) are very similar to those observed in Figure 25 (a-g). Ln_2O_3-type phases occur along the periphery of Zone 1 (Figure 26h). While these phases occur near pores, they do not appear to be located within pores. Zone 3 is composed of approximately 91 wt% U, 9 wt% Pu and less than 1 wt% Zr. A phase that contains approximately 16 wt% Pu, 8 wt% Zr and 3 wt% Mo comprises approximately 25 volume % of Zone 3. This phase is analogous to the higher Pu phase observed in lower abundances in U-19Pu-10Zr seen in Figure 25 (b-d).

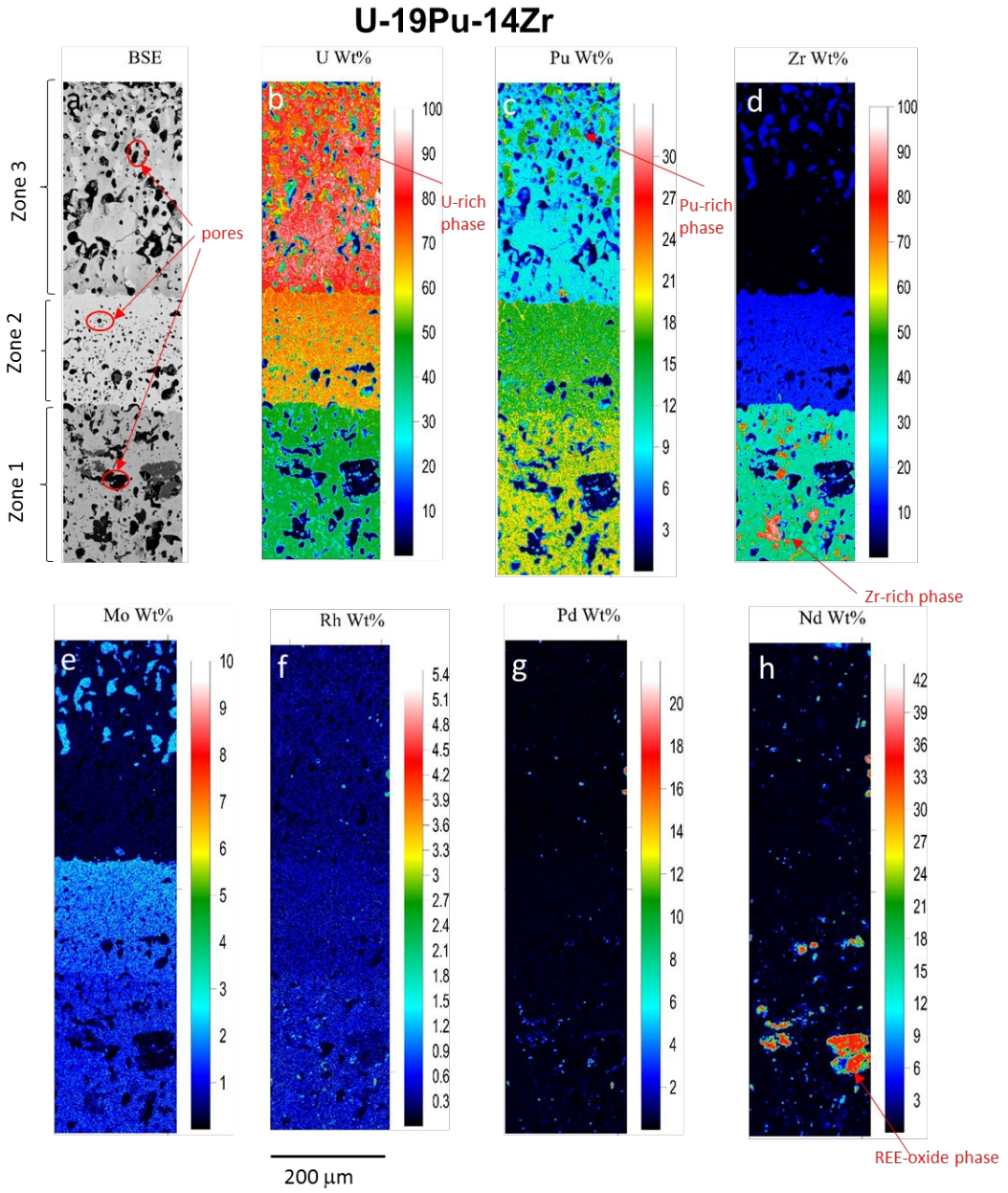

Figure 28 (a-h). a) Backscatter image of the center of U-19-14Zr; (b-h) X-ray maps of U, Pu, Zr, Mo, Rh, Pd, Nd, respectively. Mapped area is shown in Figure 18c with the black box. Note that the fuel center is toward the bottom of the images.

5.2.3 FCCI

Figure 18 (f, g), Figure 19 (f, g), and Figure 20 (f, g) show quantitative diameter X-ray maps of Nd and Pd for each of the three analyzed samples. For all three samples, Nd (which is being used to represent general lanthanide behavior) and Pd (which can form phases such as LnPd and Ln_7Pd_3 [28]) are not symmetrically distributed on both sides of the fuel-cladding interface. Instead, in all three samples they concentrate on the "west" fuel-cladding interface.

Figure 27 (a, e) shows BSE images of the fuel-cladding interface region for the "west" and "east" sides of U-19Pu-6Zr, respectively. For the "west" side of the sample, the interface is characterized by a Pu-Ln-rich layer approximately 20 μm thick. Nd begins to appear in abundance around $r/r_o = 0.6$ but is not associated with Pd until around $r/r_o = 0.8$, where its stoichiometry approximates LnPd. On the "east" side of the sample, the Pu-Ln-rich layer is approximately 10 μm thick with no observed Ln-Pd phases and Ln elements concentrated at the interface itself. The contrast can be better illustrated by examining Figure 27 (b-d, g-h). Figure 27 (c, d) shows that Am and Nd have concentration spikes near 125 μm, 250 μm, and 275 μm. Additionally, Pu concentrations plunge at those same locations. It is at these locations that the LnPd phases exist. In contrast, Figure 27 (f-h) shows no concentration apices or nadirs in the fuel. All such concentration spikes and deficits are confined to the interface only.

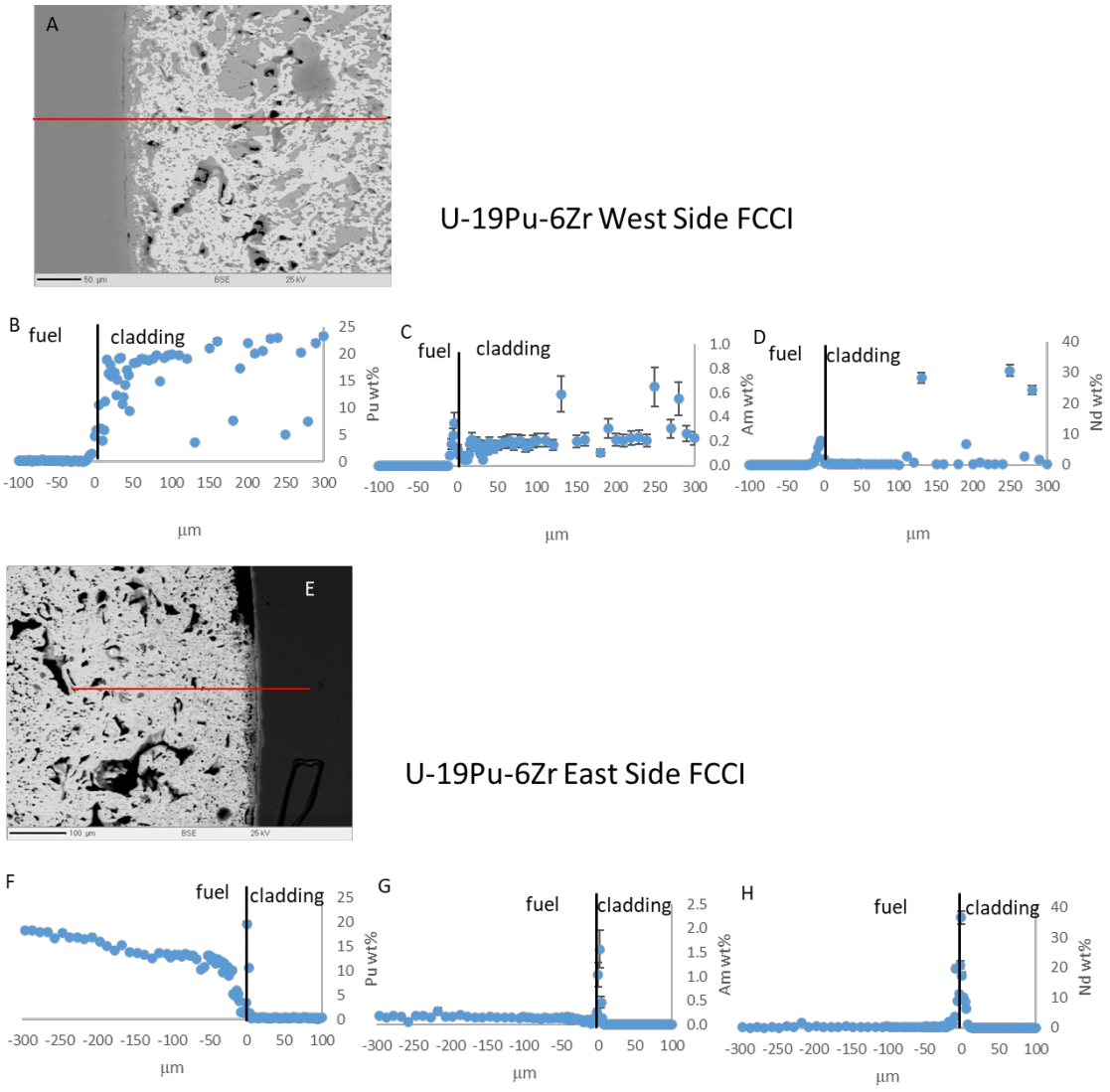

Figure 29 (a-h). a) BSE image of the FCCI region on the west side of U-19Pu-6Zr; (b-d) quantitative concentration profile (red line) across the fuel-cladding interface on the west side of U-19Pu-6Zr; e) BSE image of the FCCI region on the east side of U-19Pu-6Zr; (b-d) quantitative concentration profile (red line) across the fuel-cladding interface on the east side of U-19Pu-6Zr.

The "west" FCCI interface in U-19Pu-10Zr spans at least 50 μm across the fuel-cladding region (Figure 28b). Like the "west" side of U-19Pu-6Zr, the fuel region in this location is characterized by the presence of numerous Ln-Pd phases and a minor amount of Ln-only phases. These latter phases can appear within the center of an Ln-Pd phase, suggesting that the Ln-only phase precipitated first. In general, Pu is not especially soluble in the Ln-Pd phases as evidenced by Nd concentration elevations where Pu concentrations are low (Figure 28 [b, d]).

The "east" FCCI interface in U-19Pu-10Zr is approximately 20-30 μm thick and largely consists of Ln elements. There is no strong evidence of Ln-Pd phase formation in this location. In addition, crystal sizes are much smaller on the "east" side than on the "west" side.

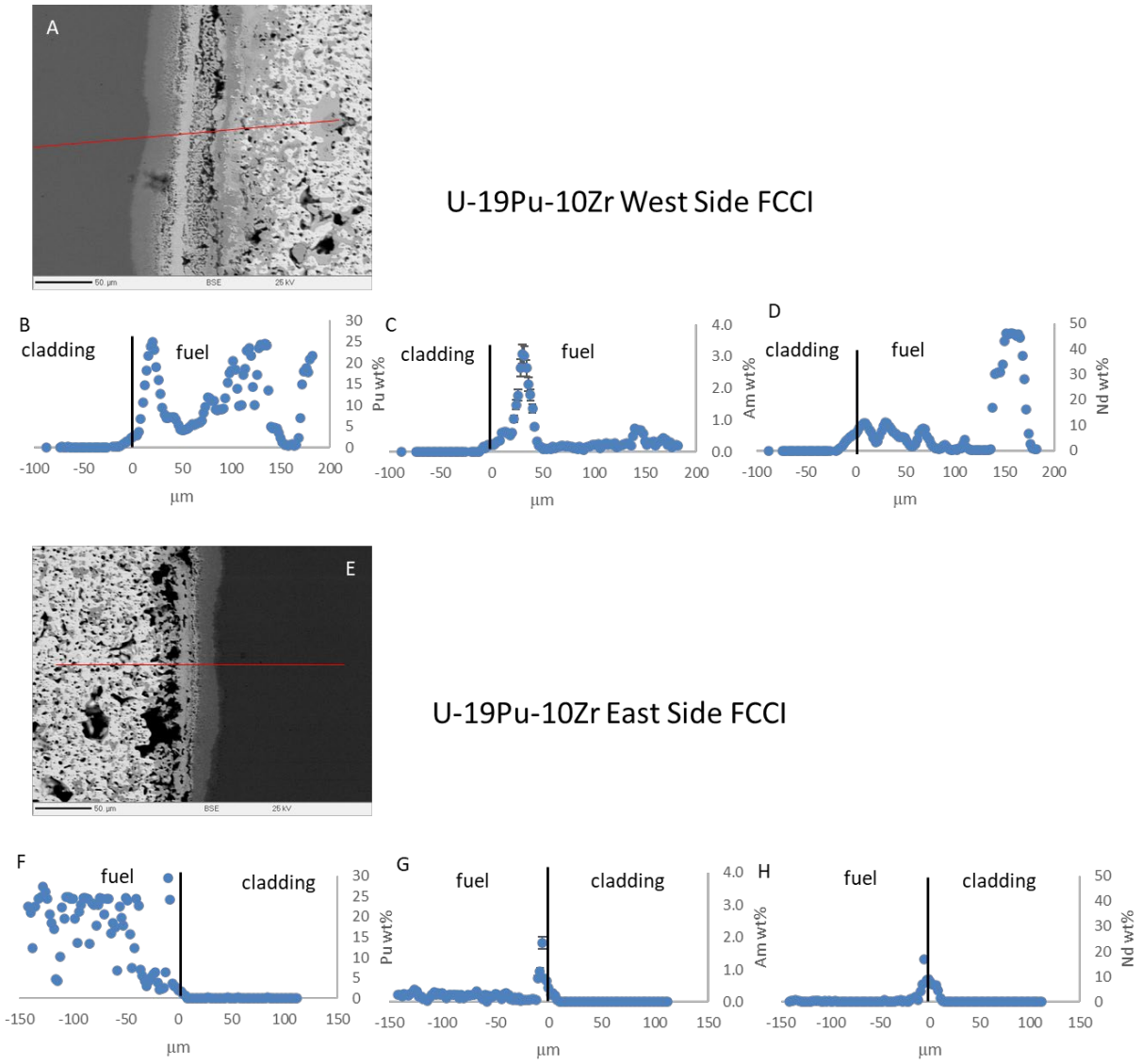

Figure 30 (a-h). a) BSE image of the FCCI region on the west side of U-19Pu-10Zr; (b-d) quantitative concentration profile (red line) across the fuel-cladding interface on the west side of U-19Pu-10Zr; e) BSE image of the FCCI region on the east side of U-19Pu-10Zr; (b-d) quantitative concentration profile (red line) across the fuel-cladding interface on the east side of U-19Pu-10Zr.

Figure 29a shows the fuel-cladding interface on the "west" side of U-19Pu-14Zr. The interaction region in this location is 60-80 µm thick, compared to 20-30 µm thick on the "east" side (Figure 29e). In contrast to the other two samples, both of sides of this sample show evidence of Ln-Pd-type phase formation.

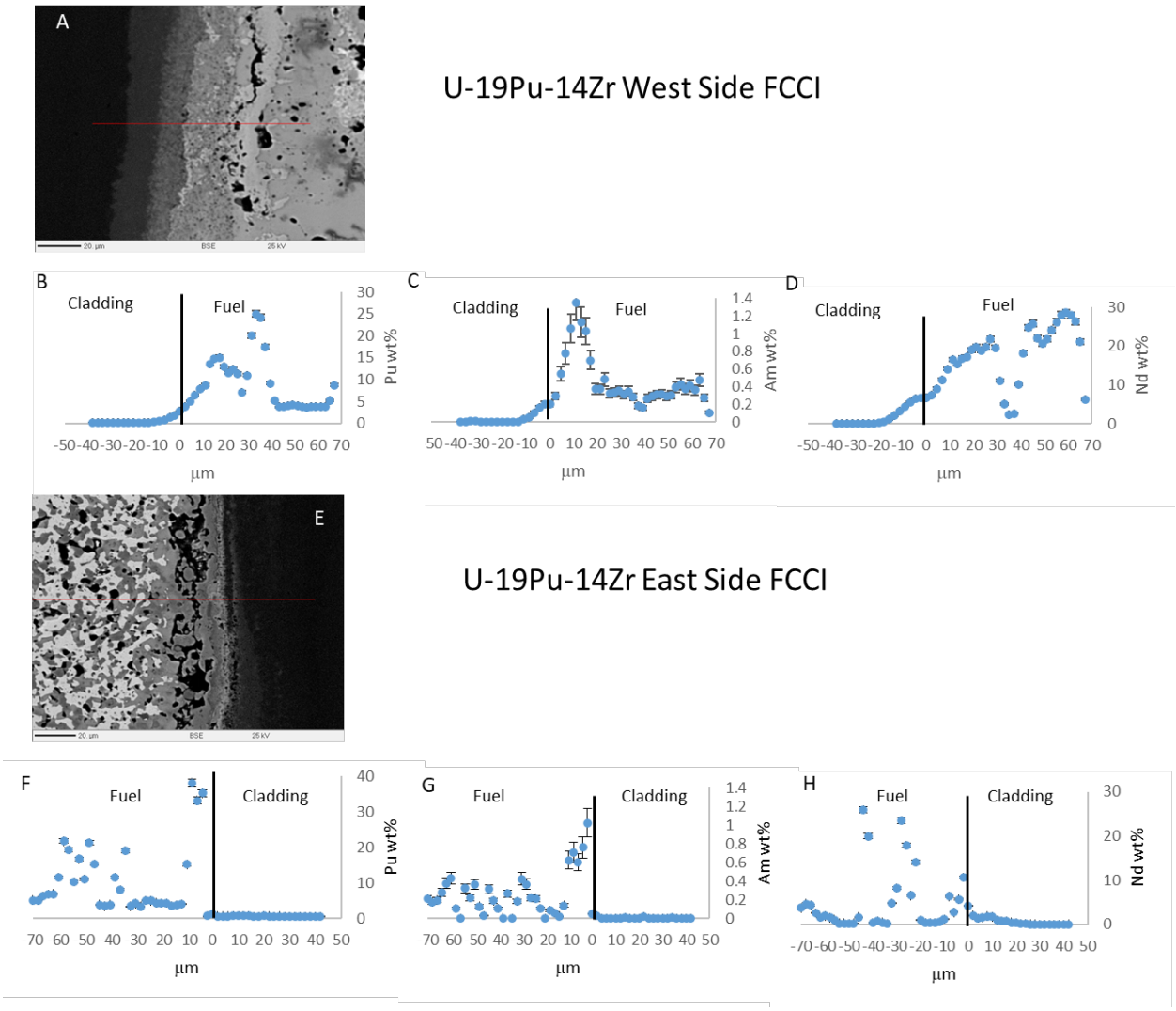

Figure 31 (a-h). a) BSE image of the FCCI region on the west side of U-19Pu-14Zr; (b-d) quantitative concentration profile (red line) across the fuel-cladding interface on the west side of U-19Pu-14Zr; e) BSE image of the FCCI region on the east side of U-19Pu-14Zr; (b-d) quantitative concentration profile (red line) across the fuel-cladding interface on the east side of U-19Pu-14Zr.

Table 7 through Table 9 show selected element penetration from fuel into cladding and from cladding into fuel for both sides of all three examined samples.

Table 7. Selected element penetration into both fuel and cladding for both sides of U-19Pu-6Zr.

Element Penetration into Cladding (µm) west Side	Element Penetration into Fuel (µm) west Side	Element Penetration into Cladding (µm) east Side	Element Penetration into Fuel (µm) east Side
U: 4	Fe: ≥ 300	U: 2	Fe: ≥ 307
Pu: ≥ 100	Cr: ≥ 300	Pu: ≥ 100	Cr: ≥ 307
Am: 10	Ni: ≥ 300	Am: 6	Ni: ≥ 307
Nd: 20	Mn: 280	Nd: 12	Mn: 157

Table 8. Selected element penetration into both fuel and cladding for both sides of U-19Pu-10Zr

Element Penetration into Cladding (μm) west Side	Element Penetration into Fuel (μm) west Side	Element Penetration into Cladding (μm) east Side	Element Penetration into Fuel (μm) east Side
U: 0	Fe: ≥ 182	U: 0	Fe: ≥ 142
Pu: ≥ 88	Cr: 180	Pu: ≥ 112	Cr: 130
Am: 10	Ni: ≥ 182	Am: 8	Ni: ≥ 142
Nd: 20	Mn: ≥ 182	Nd: 12	Mn: ≥ 142

Table 9. Selected element penetration into both fuel and cladding for both sides of U-19Pu-14Zr. "NM" indicates the element was not measured

Element Penetration into Cladding (μm) west Side	Element Penetration into Fuel (μm) west Side	Element Penetration into Cladding (μm) east Side	Element Penetration into Fuel (μm) east Side
U: 0	Fe: ≥ 67	U: 0	Fe: ≥ 74
Pu: ≥ 38	Cr: ≥ 67	Pu: ≥ 42	Cr: ≥ 74
Am: 11	Ni: ≥ 67	Am: 2	Ni: ≥ 74
Nd: 25	Mn: NM	Nd: 26	Mn: NM

Unfortunately, the same FCCI traverse length was not employed for all FCCI traverses, which complicates data interpretation. However, several trends can be discerned. U penetration into cladding only occurs in U-19Pu-6-Zr and does not exceed 4 μm. Pu penetration into cladding extended at least 38 μm (U-19Pu-14-Zr). Am and Nd cladding penetration are similar for all three samples, but Nd is slightly greater in U-19Pu-14Zr. Am and Nd penetration is greater on the "west" side compared to the "east" side of U-19Pu-6Zr (Table 7) and U-10Pu-10Zr (Table 8), but Nd penetration in U-19Pu-14Zr is approximately the same on both sides (Table 9). Ce and Nd penetrate equally on both side of all three examined samples. These tend to be followed by Pr, La, Sm, Eu, Gd, and Am, with Pr, La, and Sm being more abundant than Eu, Gd, and Am, and in some cases equal to or in similar concentration to Nd and Ce. The latter is more likely in the more Ln-rich FCCI regions.

D9 cladding is known for having large penetrations of cladding metals into the fuel (e.g., Keiser et al [29]). For both sides of U-19Pu-6Zr, Cr, Ni, and Fe penetrated at least as far as the measured traverse into the fuel—300 and 307 μm for the west and east sides, respectively. Mn penetrated 280 μm on the west side and 157 μm on the east side.

Figure 30 (a-j) shows quantitative X-ray maps of Pu and cladding elements at the fuel-cladding interface on both examined sides U-19Pu-6Zr. Figure 30b shows Fe enrichment at the "west" interface as a consequence of Ni, Cr, and Mn depletion through diffusion into the fuel. In contrast, on the "east" side, Fe shows less enrichment but rather shows more depletion, similar to Ni.

Figure 31 (a-j) shows quantitative X-ray maps of Pu and cladding elements at the fuel-cladding interface on both examined sides U-19Pu-10Zr. Figure 31a shows a strong accumulation of Pu and Fe along the boundary area between the fuel and cladding on the "west" side of the sample. This is coupled with minor accumulations of Ni, Cr, and Mn that occur adjacent to the metal depletion zone. The thickness of the Fe-rich zone between the fuel and cladding on the west side is on the order of 50-60 μm, which is similar to the Mn-layer thickness with which it co-occurs. The Pu-rich portion of that feature is on the order of 20-30 μm thick. The FCCI region on the "east" side of the sample is generally thinner than that on the "west" side (Figure 31 [f-j]) though it behaves similarly. Fe, Ni, and Mn each penetrate the

fuel on both side of the pin at least as far as the measured traverse (i.e., 182 μm on the west side and 142 μm on the east side); however, Cr penetrates only 130 μm on the east side.

Figure 32 (a-j) shows quantitative X-ray maps of Pu and cladding elements at the fuel-cladding interface on both examined sides U-19Pu-14Zr. These images show that Fe and Ni have penetrated at least 300 μm into the "west" side of the pin (Figure 32 [b, c]) with quantities of 10-15 wt% (Fe) and approximately 2 wt% (Ni). On the "east side" of the sample, Fe penetrates at least 350 μm into the fuel at concentrations of approximately 10 wt% (Figure 32f), although elevated iron concentrations are much more sporadically located than on the "west" side. In contrast, Ni concentrations of approximately 6 wt% penetrate approximately 150 μm into the "east" side (Figure 32h) of the fuel at which point the Ni concentration rapidly diminishes.

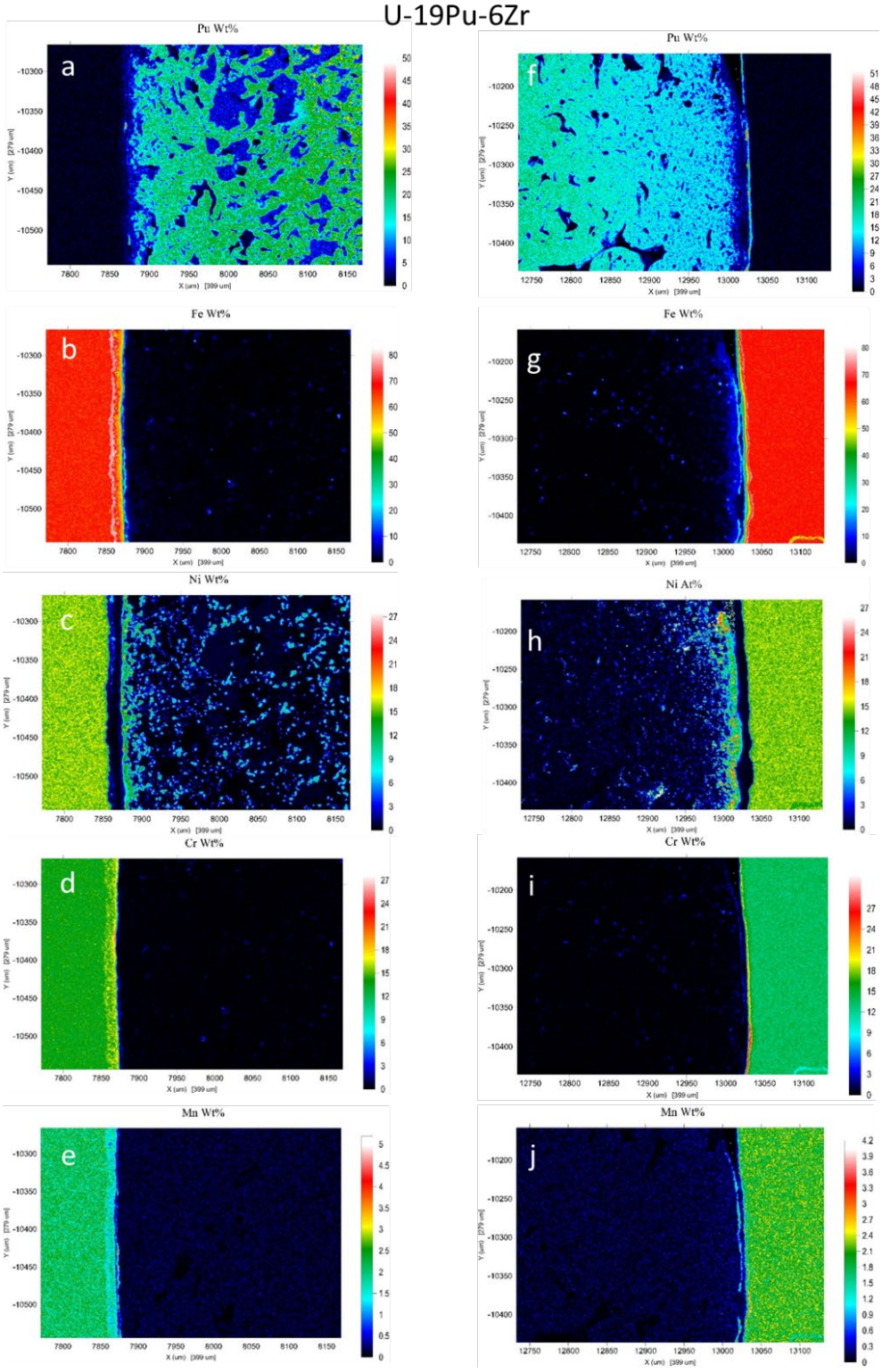

Figure 32 (a-j). (a-e) Pu and cladding elemental behavior on the "west" side of U-19Pu-6Zr; (f-j) Pu and cladding elemental behavior on the "east" side of U-19Pu-6Zr.

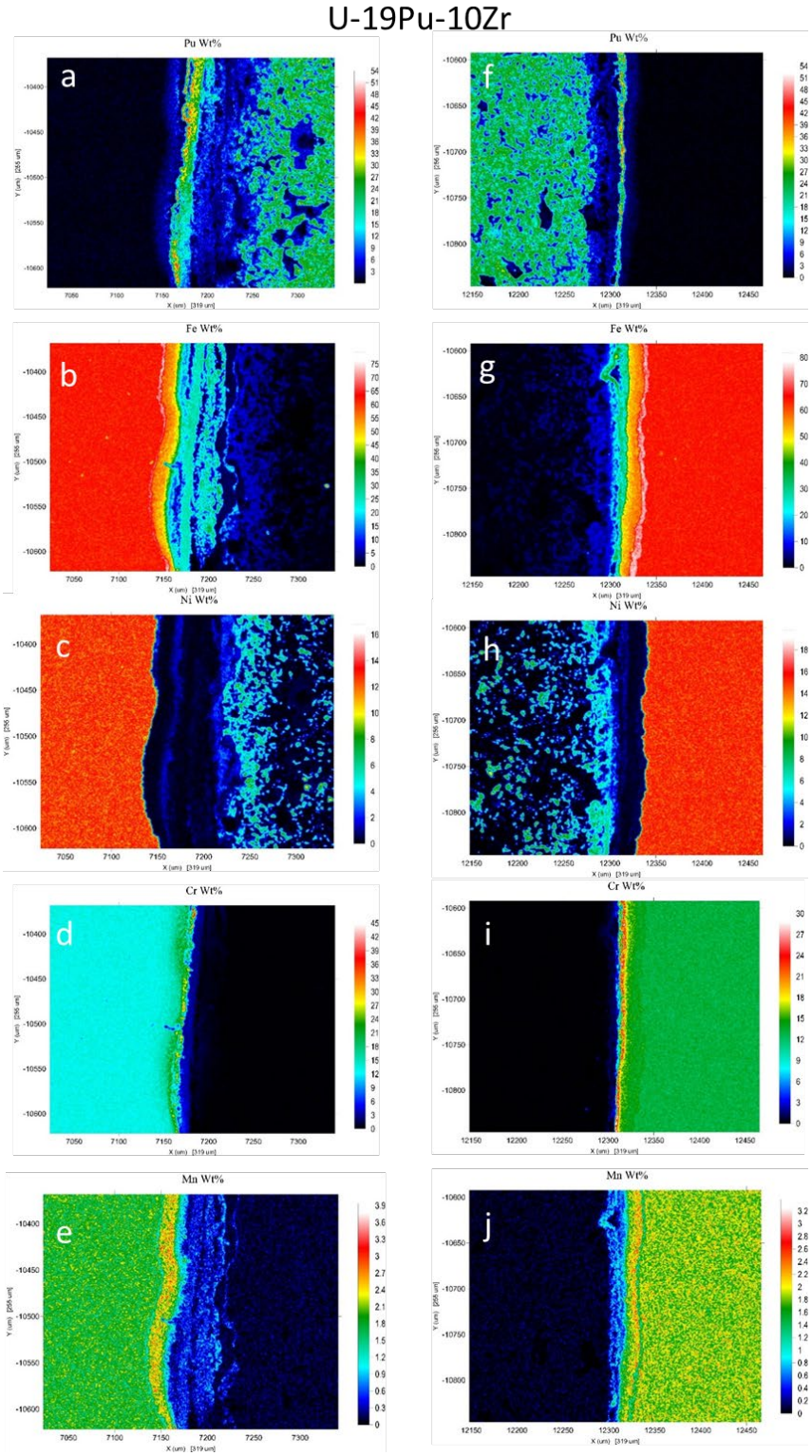

Figure 33 (a-j). (a-e) Pu and cladding elemental behavior on the "west" side of U-19Pu-10Zr; (f-j) Pu and cladding elemental behavior on the "east" side of U-19Pu-10Zr.

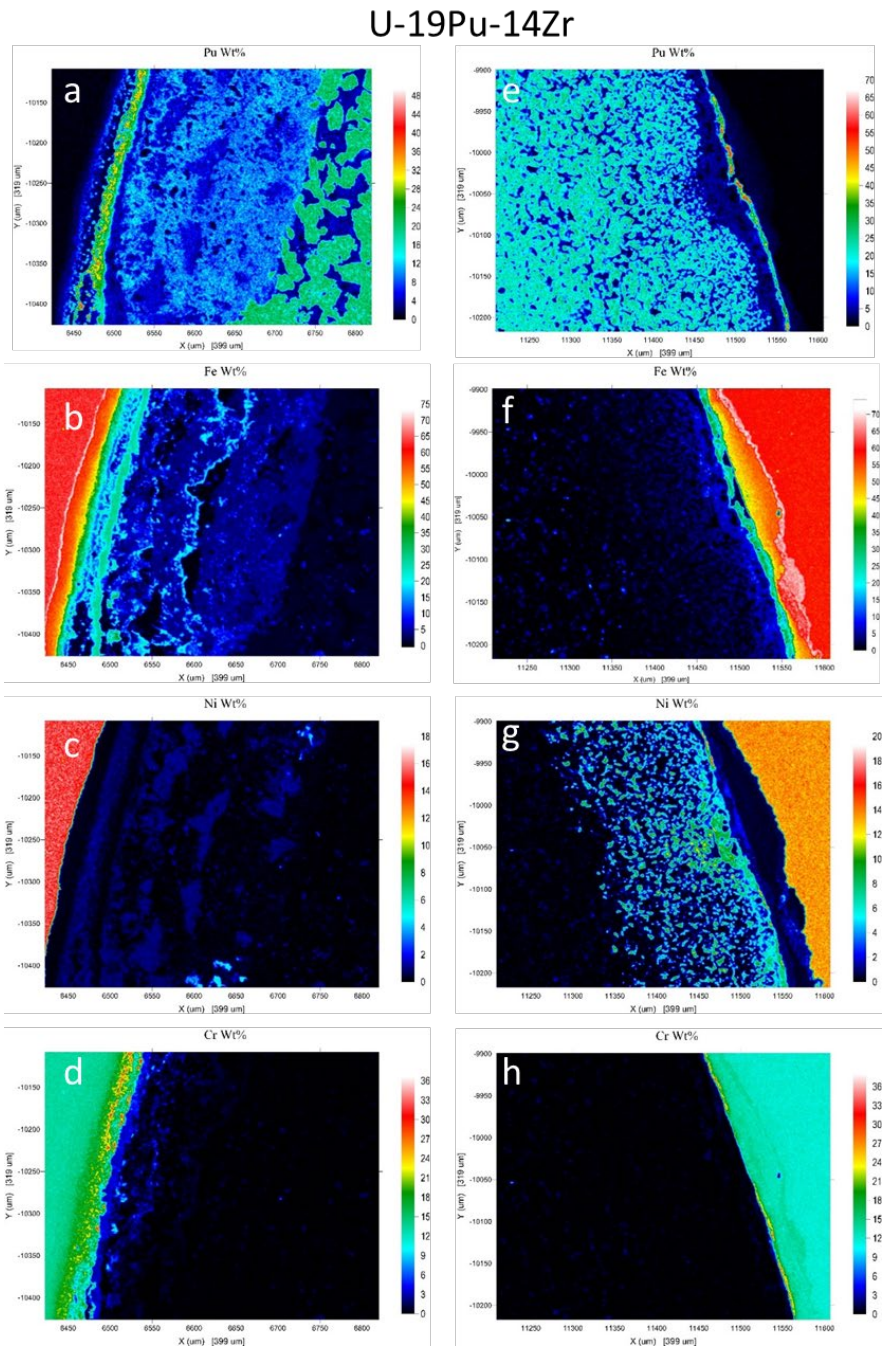

Figure 34 (a-j). (a-d) Pu and cladding elemental behavior on the "west" side of U-19Pu-14Zr; (e-h) Pu and cladding elemental behavior on the "east" side of U-19Pu-14Zr.

5.3 FIB/TEM

After completing EPMA characterization, all three fuel samples were transferred to FEI QUANTA 3D field emission gun (FEG) dual beam focused ion beam/scanning electron microscope (FIB/ SEM) to prepare lamellae for transmission electron microscopy (TEM). A total of ten lamellae were prepared from each fuel sample, and the locations were selected based on EPMA data. The lamellae were thinned at 30 kV and cleaned at 5 kV for 5minutes, and at 2 kV for 2 minutes upon completion of the thinning step. Each lamella had approximate dimensions of 20 μm × 10 μm × 0.1 μm. TEM specimens were characterized in a FEI Titan microscope operated at 300 kV. More than a hundred selective area electron diffraction (SAED) patterns were collected from the prepared lamellae to ensure all phases had been accurately captured in this analysis. Identification of formed phases was conducted by comparing experimental SAED patterns to simulated patterns from published crystal structures reproduced using SingleCrystal software. In addition, d spacing of each diffraction pattern was measured and compared to the published crystallographic data to independently verify the accuracy of the phase identification process.

For the sake of consistency between regions identified in EPMA analysis and FIB lamella locations / TEM analysis, the different regions are identified and matched in Table 10.

Table 10. Zone / region labeling matching between EPMA and FIB/TEM exams. U-19Pu-6Zr, FIB Zone C correspond to Zone 1 + Zone 2 of EPMA.

Zone EPMA	Zone FIB/TEM
Zone 1	C
Zone 2	Zone 1
Zone 3	Zone 2
Zone 4	Zone 3
FCCI	FCCI

5.3.1 U-19Pu-14Zr (A814)

Figure 33 identifies approximate locations of each lift-out prepared for U-19Pu-14Zr fuel. The locations of the lift-outs prepared for structural analysis were as closely matched to EPMA data as possible. However, the instrument used to prepare lamellae did not have BSE detector, and locations were matched visually in a secondary electron (SE) detector. SE micrographs do not provide the same level of contrast and ability to distinguish between different phases as BSE micrographs and the regions were primarily distinguished based on the porosity and general features. While the best effort was made to match precise EPMA scan locations, it was not always possible. EPMA spot size is significantly larger than the lamellae dimensions and presented data captures only small portion of the phases noted in EPMA. However, TEM data provides structural information and allows accurate determination of the phases and thus complements EPMA results.

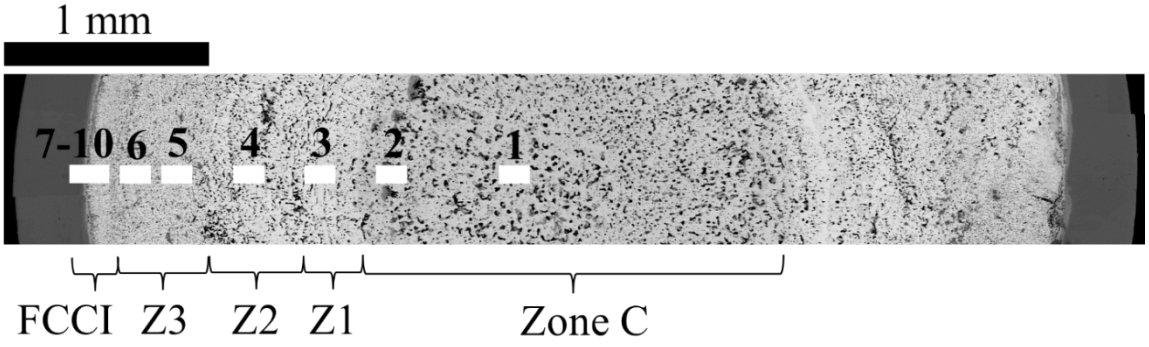

Figure 35. BSE micrograph indicating the general locations from which TEM lamella were produced for U-19Pu-14Zr fuel (see white rectangles).

In the central zone, two lift-outs (1 and 2 shown in Figure 33) were prepared and scanning TEM (STEM) micrographs from these two lift-outs are shown in Figure 34. As can be seen from Figure 34, the matrix phase was consistent with ε-Pu with β-Pu precipitates running across the matrix in both lift-outs 1 and 2. In addition, we observe precipitation of Zr in lift-out 2, which has been noted in the past. Based on EPMA results, the center region of metal fuel is enriched in Zr and the matrix phase in this region should be consistent with γ phase, commonly denoted as γ-U in published literature (a solid solution of γ-U, β-Zr, and ε-Pu) [30]. These phases are all BCC space group and have similar lattice parameters. There is a lack of experimental data available that contains structural information for the γ-phase and general assumption is that lattice parameters of γ-phase can be approximated by interpolation between the lattice parameters of pure phases. Both simulated and diffraction patterns and experimentally measured lattice spacing to all possible phases were compared, including all U and Pu allotropes, and concluded that ε-Pu is the closest match. The presence of β-Pu is not surprising because it has been observed in the past in unirradiated fuels [31,32]. This phase is not an equilibrium phase typically observed at room temperature, but can often be stabilized by impurities and therefore could be retained from the fabrication.

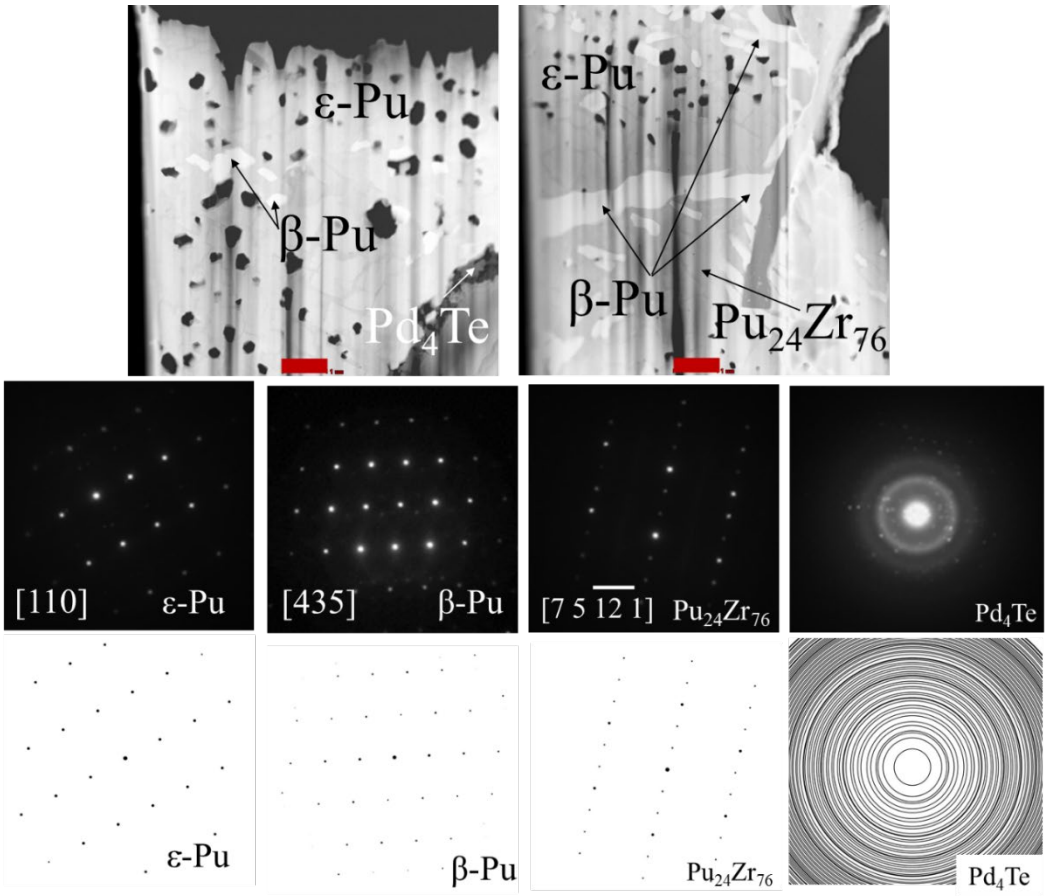

Figure 36. Selected STEM micrographs from Zone C and representative SAED patterns. Scale bars denote 1 μm.

Figure 35 depicts TEM lamella that was lifted out of Zone 1 (location 3 in Figure 33). As can be noted from Figure 35, the microstructure in Zone 1 is distinctively different from Zone C. Here, the matrix was uniform and consistent with α-(U, Pu). This region did not contain any second phase precipitates but did have several long lines running across the lamella (shown as black arrows in Figure 35). The nature of these striations is not clear as no distinctive SAED patterns could be collected from within striations due to strong contribution from the matrix phase. The presence of α-phase has been noted in the past [5,19,20] but not in the region closest to the center of the fuel.

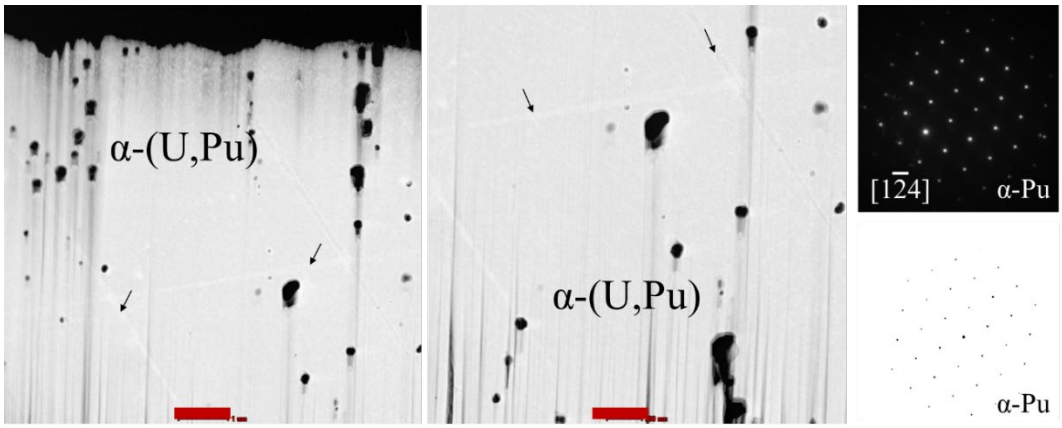

Figure 37. STEM micrographs of microstructure observed in Zone 1 and representative SAED pattern of the matrix phase. In addition to experimental SAED patterns, the match to simulated pattern is shown on the bottom right. The scale bars denote 1 μm.

Unfortunately, the lift out prepared from Zone 2 was too thick for analysis and no SAED patterns could be collected. Future work is planned to collect data from this region.

Two lamellae were prepared to characterize the microstructure of Zone 3 and the microstructure of both lift outs is shown in Figure 36. As can be seen from Figure 36, microstructure of the fuel changes significantly from Zone 1 and is more complex. The comparison is made with Zone 1 as no data was shown for Zone 2. The matrix phase in lift-out 6 was too thick, which prevented acquisition of SAED patterns but the matrix in lift-out 5 was consistent with α phase observed in Zone 1. It is possible that the matrix phase in lift-out 6 could have been consistent with δ-phase predicted by constituent redistribution model, but it is not possible to verify that, and more work will be conducted in the future. In addition to the matrix phase, several precipitates were noted that were consistent with ZrO_2, UO, UO_2, $Pu_{15}U_{85}$, and ζ-U. The presence of uranium oxides could indicate oxidation of another U-based phase but without in-situ phase identification studies, no conclusions can be made. The specimens are exposed to traces of oxygen during fabrication, assembly, and sample preparation and handling. It is possible that oxide phase was present before irradiation or formed during specimen transfer (between FIB and TEM). However, the latter is not likely as oxidation would have been noted in other lamellae and U-containing phases.

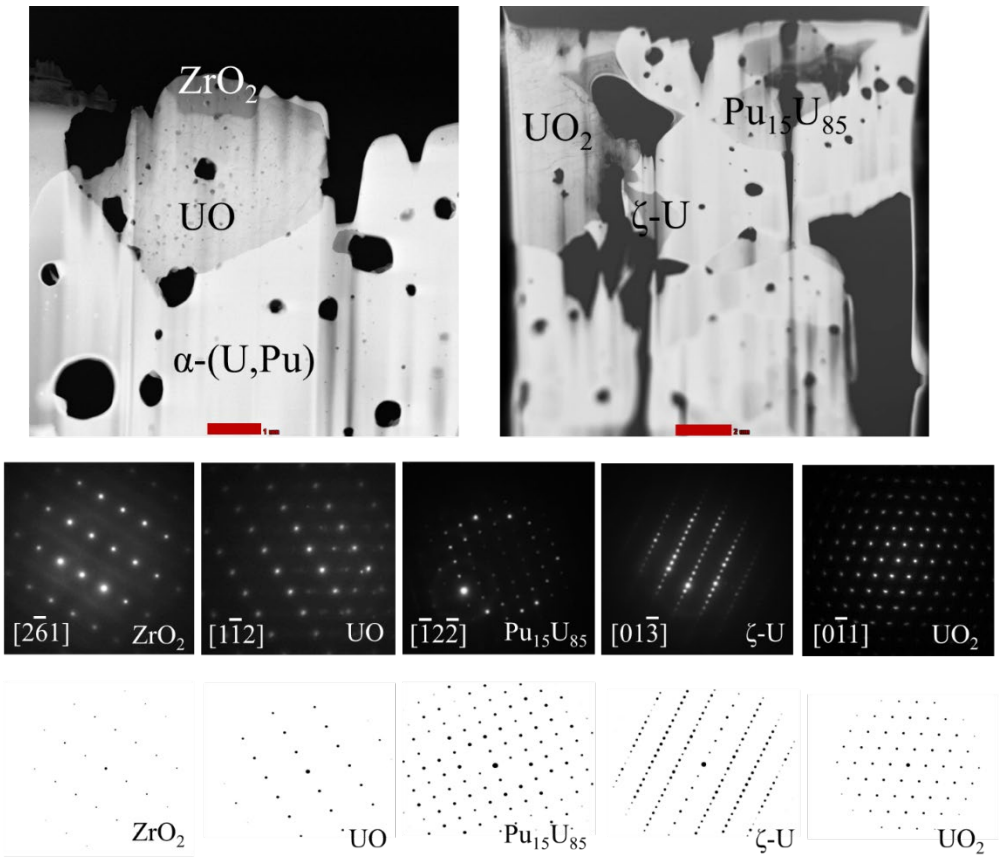

Figure 38. Selected STEM micrographs from Zone 3 and representative SAED patterns. Scale bars denote 1 μm.

In the FCCI region, three lamellae were prepared for analysis and the microstructure of the region is shown in Figure 37. Unfortunately, no matrix phases were identified because of the thinning issues in this region: matrix phase thinned at a much slower rate than precipitate phases and no SAED patterns could be collected from it. The observed secondary phases in this region included $Cr_5Fe_{24}Sm_3$, $CeCr_1$, $FeZr_2$, Pr_2Fe_{17}, $CrLaO_3$, and Fe_2U, which are all shown in Figure 37. Additional lift-outs will be prepared to capture the matrix phase.

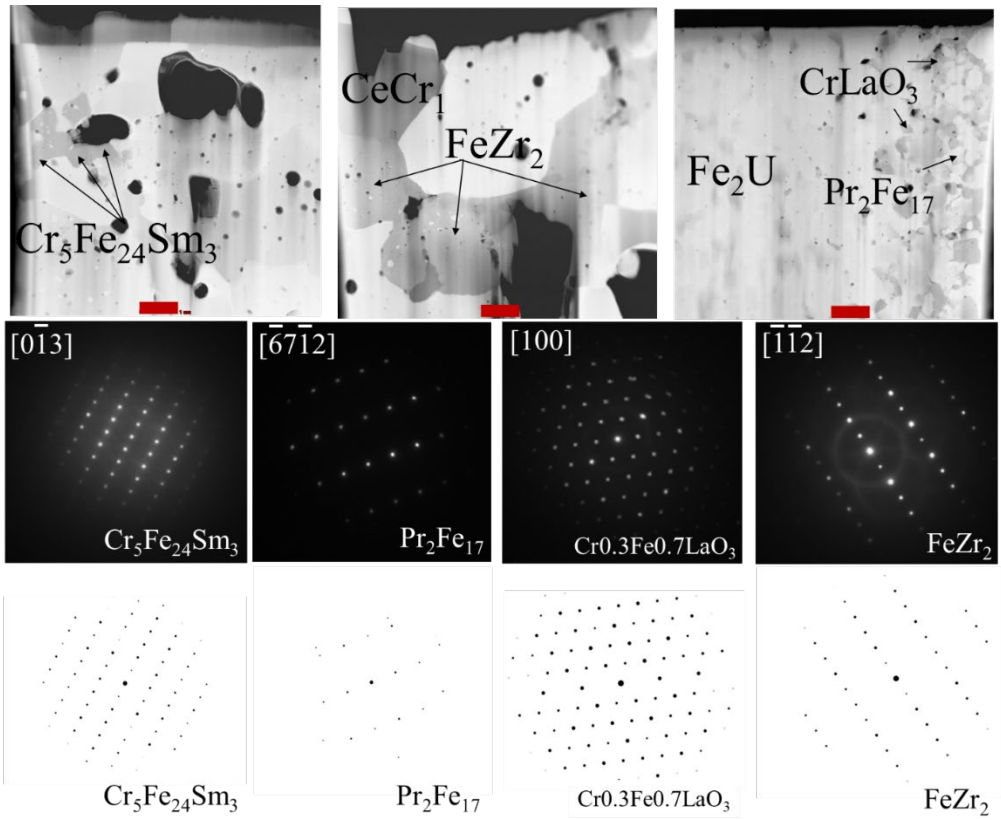

Figure 39. Selected STEM micrographs from FCCI region and representative SAED patterns. Scale bars denote 1 μm.

5.3.2 U-19Pu-10Zr (A812)

Figure 38 identifies approximate locations of each lift-out prepared for U-19Pu-10Zr fuel. Twelve lamellae were lifted-out during initial examination of the fuel. The data collection and analysis are ongoing and phase identification is incomplete at the time of writing this report. Unfortunately, of the prepared 12 lamellae, five were not appropriate for analysis (e.g., damaged during specimen transfer, not thinned sufficiently, or destroyed during preparation). These lamellae will be re-prepared for analysis (specifically, locations 4, 7, 8, 9, and 11) and re-examined.

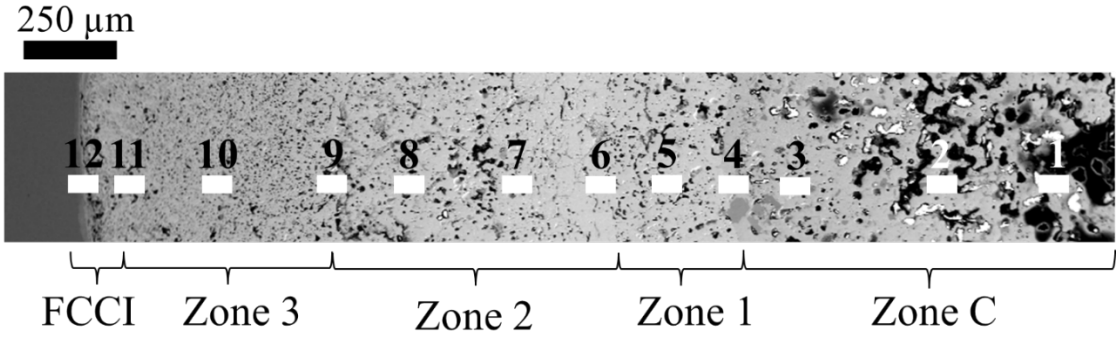

Figure 40. BSE micrograph indicating the general locations from which TEM lamella were produced from U-19Pu-10Zr fuel (see white rectangles).

5.3.3 U-19Pu-6Zr (A797)

Figure 39 identifies approximate locations of each lift-out prepared for U-19Pu-6Zr fuel. As can be seen from Figure 39, ten lift-outs were prepared from this fuel sample. Based on the analysis of the prepared samples, lift-outs 6, 7, 8, 9, and 10 were too thick for analysis and require new lift-outs.

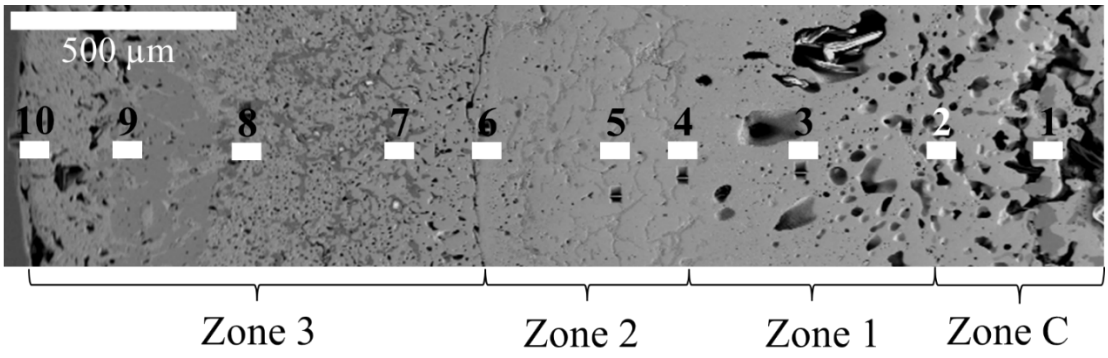

Figure 41. BSE micrograph indicating the general locations from which TEM lamella were produced from U-19Pu-6Zr fuel (see white rectangles).

In the central zone, matrix was consistent with α-(U, Pu) phase and contained β-Pu and ZrO_2 precipitates. This is contrary to the experimental observations for U-19Pu-14Zr fuel, where the matrix phase in this region was attributed to ε-Pu. The central zone in 6Zr fuel is similar to that of the Zone 1 of 14Zr fuel, where it was noted the presence of α-(U, Pu). The overview of the lamellae 1 and 2 and corresponding SAED patterns is shown in Figure 40.

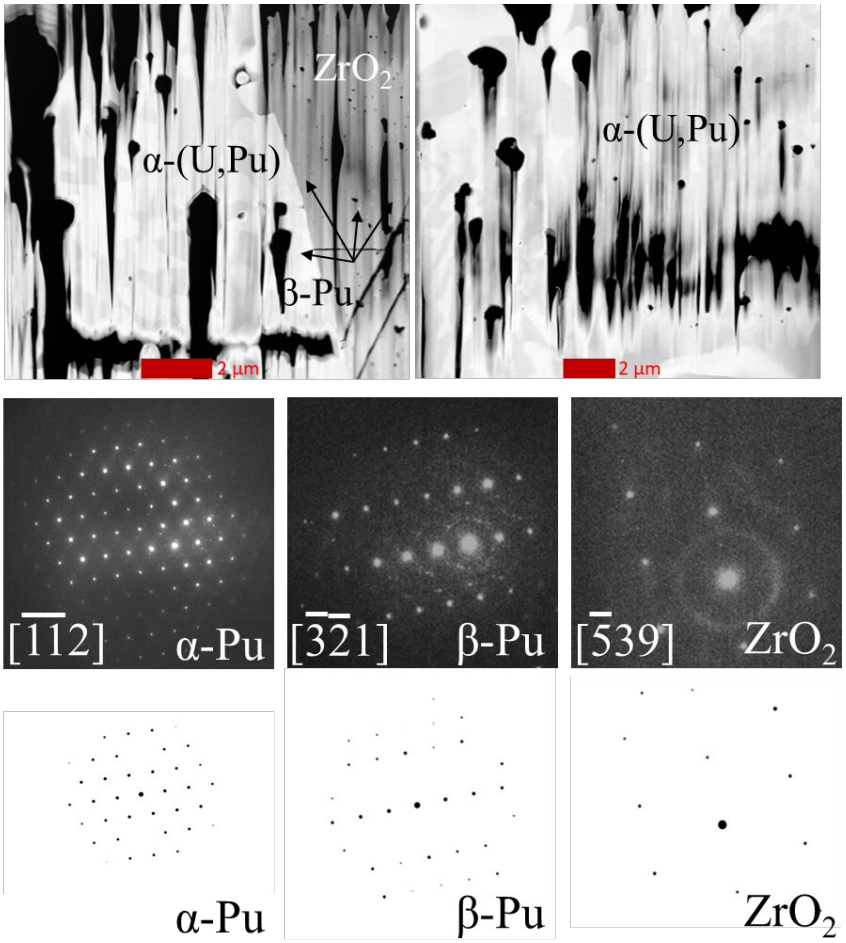

Figure 42. Selected STEM micrographs from Zone C and representative SAED patterns. Scale bars denote 1 µm.

Similar to Zone C, Zone 1 consisted of primarily α-(U, Pu) but contained a couple of regions with UO_2. This is also consistent with what has been observed for U-19Pu-14Zr fuel. The microstructure and SAED patterns of the observed phases are provided in Figure 41.

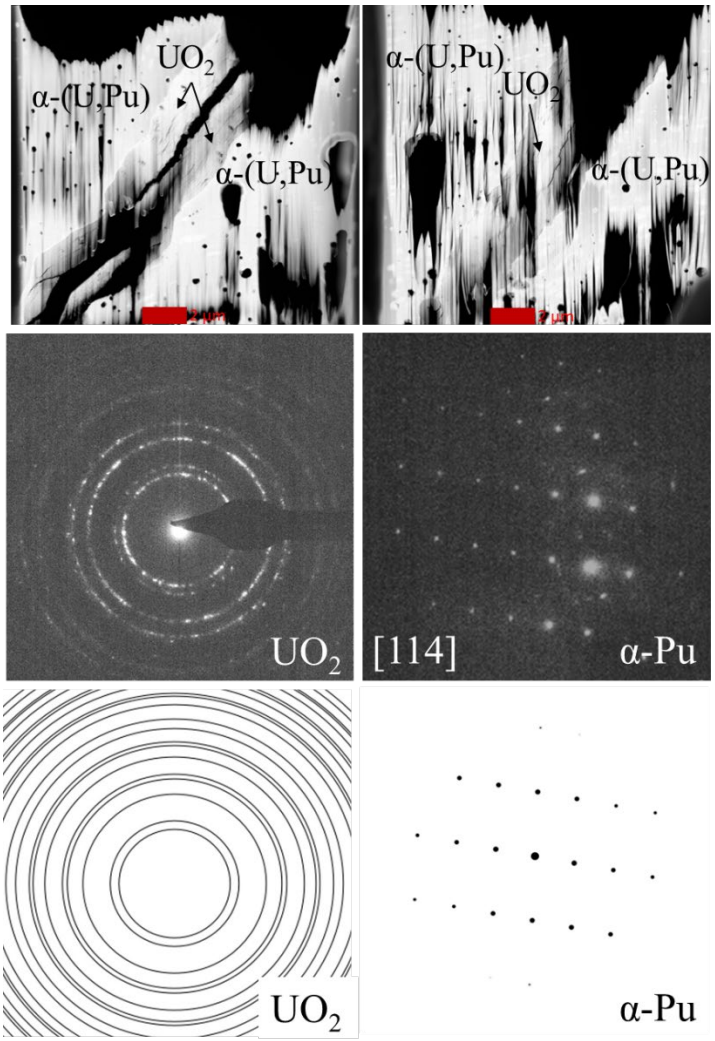

Figure 43. Selected STEM micrographs from Zone 1 and representative SAED patterns. Scale bars denote 1 μm.

In Zone 2, the matrix phase was too thick for analysis, but the examined lamellae contained secondary precipitate phases consistent with β-Pu and UO_2, which can be seen from Figure 42. It is not possible to compare these phases to those in 14Zr fuel because the lift-outs prepared from 14Zr fuel were too thick for analysis. Future comparison will be made when lift-outs from 14Zr fuel are prepared and analyzed.

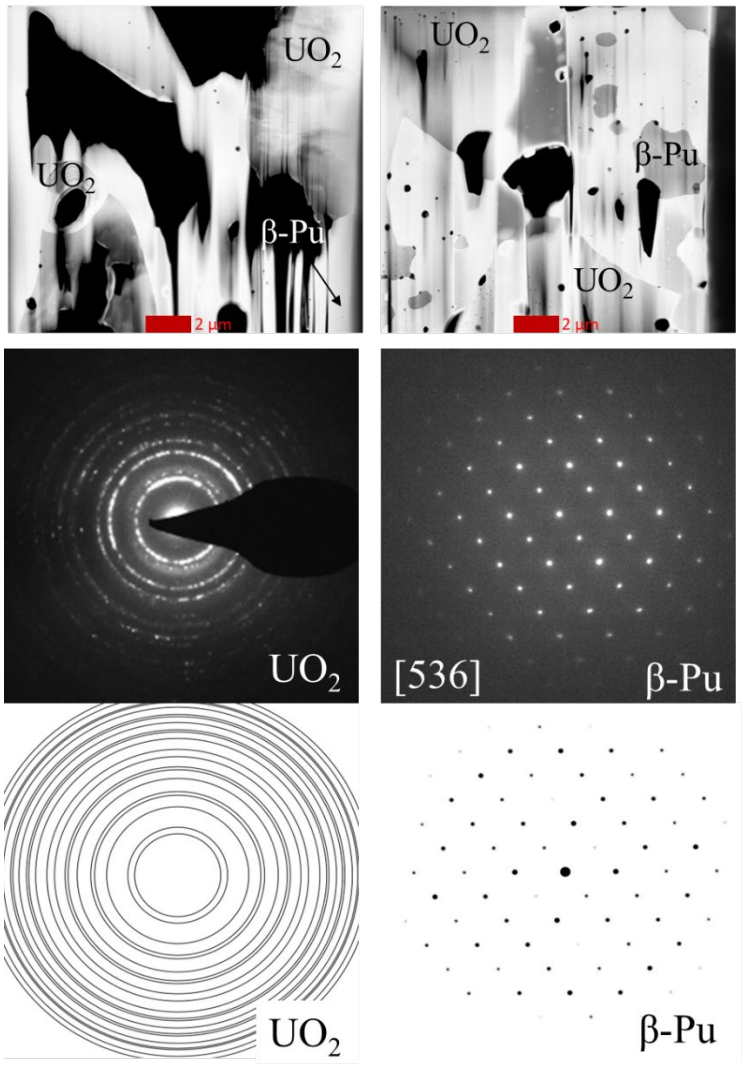

Figure 44. Selected STEM micrographs from Zone 2 and representative SAED patterns. Scale bars denote 1 µm.

Lift-outs prepared from Zone 3 were too thick for analysis and did not yield any presentable results. Additional work is planned to complete the analysis and obtain a comprehensive understanding of the phases present in these fuels. Once data collection and analysis are complete, the phases observed in each region will be compared and impact of Zr content on constituent redistribution determined.

6. ACKNOWLEDGMENT

HFEF operations and process engineers are acknowledged for the different analysis and measurements performed and data acquisition for the engineering scale PIE. EML operations is acknowledged for receiving, handling and process of the SEM samples. Jan-Fong Jue is acknowledged for scheduling and supervision of the SEM operation, as well as Alex Winston for helping with scheduling and sample preparation in SEM. IMCL operations is acknowledged for receiving, handling, and process of the samples for EPMA and FIB/TEM analysis. Fei Teng is thanked for supporting preparation of the lamellae in the FIB along with Daniel Murray and Lingfeng He for scheduling instrument time (FIB and TEM).

Finally, Collin Knight is acknowledged for overall managing and finance of the project as NSUF PIE program manager.

7. REFERENCES

[1] N.L.A. Tsai H, Cohen A B; Billone M C, Irradiation Performance of U-Pu-Zr metal fuels for liquid-metal cooled reactors, in: 3rd Intl. Conf. Nucl. Enginnering, 1995.

[2] H.B.M.C. Tsai, Data package for the irradiation of the DP-1 test (X441) in EBR-II, Argonne Natl. Lab. Intra-Laboratory Memo. (1987).

[3] G.L. Hofman, L.C. Walters, T.H. Bauer, Metallic fast reactor fuels, Prog. Nucl. Energy. 31 (1997) 83–110. https://doi.org/10.1016/0149-1970(96)00005-4.

[4] T. Ogata, Metal Fuel, in: Compr. Nucl. Mater., Elsevier, 2012: pp. 1–40. https://doi.org/10.1016/B978-0-08-056033-5.00049-5.

[5] G.L. Hofman, R.G. Pahl, C.E. Lahm, D.L. Porter, Swelling behavior of U-Pu-Zr fuel, Metall. Trans. A. (1990). https://doi.org/10.1007/BF02671924.

[6] D.L.L. Porter, H. Tsai, Full-length U–xPu–10Zr (x =0, 8, 19wt.%) fast reactor fuel test in FFTF, J. Nucl. Mater. 427 (2012) 46–57. https://doi.org/10.1016/j.jnucmat.2012.03.047.

[7] H.B.M. c Tsai, DP-1 Pin Cladding strain data as related to the Mk-V fuel design, 1990.

[8] R.G. Pahl, D.L. Porter, D.C. Crawford, L.C. Walters, Irradiation behavior of metallic fast reactor fuels, J. Nucl. Mater. (1992). https://doi.org/10.1016/0022-3115(92)90447-S.

[9] J.M. Harp, P.A. Demkowicz, Investigation of the Feasibility of Utilizing Gamma Emission Computed Tomography in Evaluating Fission Product Migration in Irradiated TRISO Fuel Experiments, in: Int. Top. Meet. High Temp. React. Technol. (HTR 2014), 2014.

[10] J.D. Hunn, C.A. Baldwin, T.J. Gerczak, F.C. Montgomery, R.N. Morris, C.M. Silva, P.A. Demkowicz, J.M. Harp, S.A. Ploger, Detection and analysis of particles with failed SiC in AGR-1 fuel compacts, Nucl. Eng. Des. (2016). https://doi.org/10.1016/j.nucengdes.2015.12.011.

[11] J.M. Harp, H.J.M. Chichester, L. Capriotti, Postirradiation examination results of several metallic fuel alloys and forms from low burnup AFC irradiations, J. Nucl. Mater. 509 (2018) 377–391. https://doi.org/10.1016/J.JNUCMAT.2018.07.003.

[12] J.M. Harp, L. Capriotti, H.J.M. Chichester, Postirradiation Examination of FUTURIX-FTA metallic alloy experiments, J. Nucl. Mater. 515 (2019) 420–433. https://doi.org/10.1016/J.JNUCMAT.2018.12.051.

[13] W.J. Maeck, R.P. Larsen, J.E. Rein, Burnup Determination for Fast Reactor Fuels: A Review and Status of the Nuclear Data and Analytical Chemistry Methodology Requirements, U.S. At. Energy Comm. TID-26209 (1973).

[14] J.M. Harp, P.A. Demkowicz, P.L. Winston, J.W. Sterbentz, An analysis of nuclear fuel burnup in the AGR-1 TRISO fuel experiment using gamma spectrometry, mass spectrometry, and computational simulation techniques, Nucl. Eng. Des. 278 (2014) 395–405. https://doi.org/10.1016/j.nucengdes.2014.07.041.

[15] M.B. Chadwick, M. Herman, P. Obložinský, M.E. Dunn, Y. Danon, A.C. Kahler, D.L. Smith, B. Pritychenko, G. Arbanas, R. Arcilla, R. Brewer, D.A. Brown, R. Capote, A.D. Carlson, Y.S. Cho, H. Derrien, K. Guber, G.M. Hale, S. Hoblit, S. Holloway, T.D. Johnson, T. Kawano, B.C. Kiedrowski, H. Kim, S. Kunieda, N.M. Larson, L. Leal, J.P. Lestone, R.C. Little, E.A. McCutchan, R.E. MacFarlane, M. MacInnes, C.M. Mattoon, R.D. McKnight, S.F. Mughabghab, G.P.A. Nobre, G. Palmiotti, A. Palumbo, M.T. Pigni, V.G. Pronyaev, R.O. Sayer, A.A. Sonzogni, N.C. Summers, P. Talou, I.J. Thompson, A. Trkov, R.L. Vogt, S.C. van der Marck, A. Wallner, M.C. White, D. Wiarda, P.G. Young, ENDF/B-VII.1 Nuclear Data for Science and Technology: Cross Sections, Covariances, Fission Product Yields and Decay Data, Nucl. Data Sheets. 112 (2011) 2887–2996. https://doi.org/10.1016/J.NDS.2011.11.002.

[16] G.L. Hofman, W.N. Beck, R. V Strain, G.O. Hayner, C.M. Walter, Irradiation Behavior of Unencapsulated EBR-II Mark-II Driver Fuel to a Maximum Burnup of 6 at.%, ANL-8119, Argonne Natl. Lab. (1976).

[17] G.L. Hofman, S.L. Hayes, M.C. Petri, Temperature gradient driven constituent redistribution in U□Zr alloys, J. Nucl. Mater. 227 (1996) 277–286. https://doi.org/10.1016/0022-3115(95)00129-8.

[18] W.J. Carmack, D.L. Porter, Y.I. Chang, S.L. Hayes, M.K. Meyer, D.E. Burkes, C.B. Lee, T. Mizuno, F. Delage, J. Somers, Metallic fuels for advanced reactors, J. Nucl. Mater. 392 (2009) 139–150. https://doi.org/10.1016/J.JNUCMAT.2009.03.007.

[19] Y.S. Kim, G.. Hofman, S.. Hayes, Y.. Sohn, Constituent redistribution in U–Pu–Zr fuel during irradiation, J. Nucl. Mater. 327 (2004) 27–36. https://doi.org/10.1016/J.JNUCMAT.2004.01.012.

[20] D.E. Janney, Metallic Fuels Handbook, Part 1 and Part 2, Idaho Natl. Lab. Rep. (2018) INL/EXT-15-36520 r.3. https://doi.org/10.2172/1469797.

[21] L. Capriotti, S. Brémier, K. Inagaki, P. Pöml, D. Papaioannou, H. Ohta, T. Ogata, V. V. Rondinella, Characterization of metallic fuel for minor actinides transmutation in fast reactor, Prog. Nucl. Energy. 94 (2017) 194–201. https://doi.org/10.1016/j.pnucene.2016.04.004.

[22] L. Capriotti, J.M. Harp, Characterization of a minor actinides bearing metallic fuel pin irradiated in EBR-II, J. Nucl. Mater. 539 (2020). https://doi.org/10.1016/j.jnucmat.2020.152279.

[23] J.M. Harp, D.L. Porter, B.D. Miller, T.L. Trowbridge, W.J. Carmack, Scanning electron microscopy examination of a Fast Flux Test Facility irradiated U-10Zr fuel cross section clad with HT-9, J. Nucl. Mater. 494 (2017) 227–239. https://doi.org/10.1016/j.jnucmat.2017.07.040.

[24] D.D. Keiser, Fuel-Cladding Interaction Layers in Irradiated U-Zr and U-Pu-Zr Fuel Elements, ANL-NT-240, Argonne National Laboratory, Chicago, United States, 2006. https://doi.org/10.2172/885496.

[25] K.E. Wright, J.M. Harp, L. Capriotti, Electron Probe Microanalysis of Irradiated FUTURIX-FTA U-Pu-Zr Alloy with Added Minor Actinides, J. Nucl. Mater. (n.d.) under review.

[26] J.-L. Pouchou, F. Pichoir, Quantitative Analysis of Homogeneous or Stratified Microvolumes Applying the Model “PAP,” in: Electron Probe Quant., 1991. https://doi.org/10.1007/978-1-4899-2617-3_4.

[27] I.R. Farthing, C.T. Walker, Heinrich’s Mass Absorption Coefficients for the K, L, and M Lines, Eur. Comm. Inst. Transuranium Elem. Karlsruhe,. (1990).

[28] M.T. Benson, J.M. Harp, Y. Xie, T. Yao, K.R. Tolman, K.E. Wright, J.A. King, A.I. Hawari, Q. Cai, Out-of-pile and postirradiated examination of lanthanide and lanthanide-palladium interactions for metallic fuel, J. Nucl. Mater. 544 (2021) 152727. https://doi.org/10.1016/j.jnucmat.2020.152727.

[29] D.D. Keiser, Metal fuel-cladding interaction, in: Compr. Nucl. Mater., 2012. https://doi.org/10.1016/B978-0-08-056033-5.00067-7.

[30] D. Janney, C. Adkins, S. Hayes, A Critical Review of the Experimentally Known Properties of U-Pu-Zr Alloys. Part 1: Phases and Phase Diagrams, Nucl. Technol. (2019). https://doi.org/10.1080/00295450.2019.1578573.

[31] A. Aitkaliyeva, C.A. Adkins, J. Hirschhorn, C. McKinney, M.R. Tonks, F.G. Di Lemma, Microstructural characterization of the as-cast and annealed Pu-10Zr alloy, J. Nucl. Mater. 523 (2019). https://doi.org/10.1016/j.jnucmat.2019.05.051.

[32] E. King, J.A. Lee, The low temperature resistivity of β-phase plutonium, Cryogenics (Guildf). 3 (1963). https://doi.org/10.1016/0011-2275(63)90013-4.